Microdosimetry of radiohalogens in thyroid models

Anders Josefsson

Department of Radiation Physics

Institute of Clinical Sciences

Sahlgrenska Academy at University of Gothenburg

UNIVERSITY OF GOTHENBURG

Gothenburg 2014

Microdosimetry of radiohalogens in thyroid models

ISBN 978-91-628-8915-9
http://hdl.handle.net/2077/34811
Printed by Kompendiet, Gothenburg, Sweden

Everything happens for a reason and that reason is usually physics

Microdosimetry of radiohalogens in thyroid models

Anders Josefsson

Department of Radiation Physics, Institute of Clinical Sciences,
Sahlgrenska Academy at University of Gothenburg, Gothenburg, Sweden, 2014

ABSTRACT

The radiohalogens ^{123}I, ^{124}I, ^{125}I, ^{131}I, and ^{211}At are routinely used or proposed for diagnostic and therapeutic purposes. The different characteristics and application areas of these radioiodine isotopes, together with the possibility to bind them to the same carrier molecule, give many advantages, for example, by enabling relevant biodistribution and dosimetric studies important for dose-planning before radionuclide therapy. ^{211}At, with its relatively long half-life, stable daughter nuclide, and production and labelling possibilities is considered as one of the most attractive alpha particle emitters in radionuclide therapy. With growing use of radiohalogens in both preclinical and clinical studies there is a need for accurate species-specific dosimetric models both for tumours and normal tissues. The thyroid gland has shown a high uptake of radioiodide and free ^{211}At and is, therefore, considered as an organ at risk. It is thus critical to be able to accurately calculate the absorbed dose in the thyroid. Accurate dosimetry is also important for radiation protection purposes for personnel handling radiohalogens and for populations exposed to radioiodine, e.g., at a nuclear accident.

The MIRD formalism is commonly used for calculating the mean absorbed dose, assuming a homogeneous distribution of the radionuclide within the thyroid gland. Several studies have shown heterogeneous distribution of radioiodine and ^{211}At within the thyroid gland.

In this work, geometrical models were developed for different species: man, rat and mouse. Microdosimetric calculations for heterogeneous distributions of the different radiohalogens in these thyroid models were performed using MCNPX Monte Carlo code and recent nuclear decay data. The results showed large differences in mean absorbed dose compared with MIRD formalism.

The heterogeneity in absorbed dose within the thyroid depends on the type and energy of the emitted particles. For example, ^{131}I emits high-energy beta particles with range up to 2 mm in tissue, where the absorbed dose distribution within the thyroid is less dependent on the radionuclide distribution. On the other hand, for ^{211}At emitting alpha particles with short range in tissue (48-70 μm), and for ^{125}I emitting Auger electrons with very short range in tissue (from a fraction of a nm up to 20 μm), the absorbed dose distribution will be more dependent on the radiohalogen distribution.

The results also demonstrate the importance of using species-specific models for dosimetric calculations for thyroid and other heterogeneous tissues, enabling dosimetric translations between different species.

Keywords: microdosimetry, Monte Carlo, radiohalogens, radioiodine, astatine-211, thyroid gland, man, rat, mouse

ISBN: 978-91-628-8915-9
E-publication: http://hdl.handle.net/2077/34811

LIST OF PAPERS

This thesis is based on the following papers, which will be referred to by their Roman numerals.

I. Anders Josefsson and Eva Forssell-Aronsson
Microdosimetric analysis of the radiohalogens ^{123}I, ^{124}I, ^{125}I, ^{131}I and ^{211}At
Submitted

II. Anders Josefsson and Eva Forssell-Aronsson
Microdosimetric analysis of ^{211}At in thyroid models for man, rat and mouse
EJNMMI Research 2012, **2**:29

III. Anders Josefsson and Eva Forssell-Aronsson
Microdosimetric modelling of ^{123}I, ^{125}I and ^{131}I in thyroid follicle models
Submitted

Preliminary results have been presented as follows

Josefsson A. and Forssell-Aronsson E.
Microdosimetric analysis of ^{211}At in thyroid (follicle) model
Poster presentation at the European Radiation Research 2010 (ERR2010), September 5-9, 2010, Stockholm, Sweden

Josefsson A. and Forssell-Aronsson E.
MC-simulations of ^{211}At decay in a thyroid (follicle) model using MCNPX
Poster presentation at the International workshop in Monte Carlo technic (MC2010), November 9-12, 2010, Stockholm, Sweden

Josefsson A. and Forssell-Aronsson E.
MC-simulations of ^{211}At dosimetry in a thyroid (follicle) model using MCNPX
Oral presentation at the Oncological Nuclide Therapy Meeting supported by the Swedish Cancer Society, November 18-19, 2010, Lund, Sweden

Josefsson A. and Forssell-Aronsson E.
^{211}At dosimetry in a thyroid model using MCNPX
Oral presentation at the TARCC International Congress: Advances in targeted radionuclide therapy, December 1-2, 2010, Ljubljana, Slovenia

Josefsson A. and Forssell-Aronsson E.
Microdosimetric analysis of ^{211}At in a thyroid (follicle) model
Oral presentation at the 7th Symposium on Targeted Alpha Therapy, July 18-19, 2011, Berlin, Germany

Josefsson A. and Forssell-Aronsson E.
Microdosimetric modelling of thyroid follicles for ^{211}At
Oral presentation at the Annual Congress of the European Association of Nuclear Medicine (EANM 2011), October 15-19, 2011, Birmingham, United Kingdom

Josefsson A. and Forssell-Aronsson E.
Comparison of microdosimetric parameters between ^{211}At and the radioiodine isotopes ^{123}I, ^{125}I and ^{131}I in thyroid (follicle) models
Poster presentation at the 8th Symposium on Targeted Alpha Therapy, June 4-6, 2013, Oak Ridge, TN, USA

Josefsson A. and Forssell-Aronsson E.
Microdosimetric analysis of ^{123}I, ^{125}I and ^{131}I in thyroid (follicle) models
Oral presentation at the Annual Meeting of the Society of Nuclear Medicine and Molecular Imaging (SNMMI 2013), June 8-12, 2013, Vancouver, BC, Canada

TABLE OF CONTENTS

ABBREVIATIONS

AE	Auger, Coster-Kronig and super Coster-Kronig electrons
CE	Internal Conversion Electron
CK	Coster-Kronig and super Coster-Kronig electrons
CSDA	Continuous Slowing Down Approximation
$\overline{D}_{MIRD}$	Mean absorbed dose calculated according to MIRD formalism
$\overline{D}_{PW}$	Mean absorbed dose calculated in present work (PW)
DNA	Deoxyribonucleic acid
EC	Electron Capture
Gy	Gray, SI unit of absorbed radiation dose (1 Gy = 1 J/kg)
ICRP	International Commission on Radiation Protection
ICRU	International Commission on Radiation Units and Measurements
IT	Isomeric Transition
LCGRNG	Linear Congruential Random Number Generator
LET	Linear Energy Transfer
MCNP	Monte Carlo N-Particle
MCNPX	Monte Carlo N-Particle eXtended
MFP	Mean Free Path
MIRD	Medical Internal Radiation Dose
NIS	Sodium Iodide Symporter
NR	Non-Radiative
PET	Positron Emission Tomography
PDF	Probability Density Function
PRNG	Pseudo-Random Number Generator
R_{CSDA}	Continuous Slowing Down Approximation Range
SNMMI	The Society of Nuclear Medicine and Molecular Imaging
SPECT	Single Photon Emission Computed Tomography
Tg	Thyroglobulin
T_3	Triiodothyronine
T_4	Thyroxine
$\langle z \rangle$	Mean specific energy

1. INTRODUCTION

The first successful treatment of metastatic thyroid carcinoma using the radioiodine isotope ^{131}I was reported in 1946 [1]. Today the radioiodine isotopes ^{123}I, ^{124}I, ^{125}I and ^{131}I are frequently used or proposed for diagnostic and therapeutic applications. The different characteristics and application areas of the radioiodine isotopes, and the possibility that they can be to be bound to the same carrier molecules, gives many advantages for example by enabling biodistribution and dosimetric studies important for treatment-planning before radionuclide therapy. In 1954 for the first, and to my knowledge, the only time tracer amounts of free ^{211}At was administered to 8 patients, suffering from various thyroid disorders [2]. Today, the alpha particle emitter ^{211}At, bound to tumour-seeking agents, shows promising results for therapy of micrometastases in ovarian cancer and for brain cancer [3, 4]. ^{211}At is considered one of the most attractive alpha particle emitter in radionuclide therapy, with its relatively long half-life of 7.2 hours, stable daughter nuclide [5] and production possibilities [6]. With this growing use of radiohalogens in both preclinical and clinical studies there is a need for accurate species-specific dosimetric models, both for tumours and critical normal tissues. The thyroid gland has shown a high uptake of unbound radioiodide and ^{211}At [2, 7-12], and is therefore an organ at risk. It is thus important with accurate dosimetric calculations of the absorbed dose to thyroid from ionising radiation from radiohalogens, when evaluating the risks in case of exposure, in diagnostics and therapy and in preclinical studies. Accurate dosimetry is also important for radiation protection purposes for personnel handling radiohalogens and for populations exposed to radioiodine, e.g. at a nuclear accident.

1.1 THE THYROID GLAND

The thyroid is an endocrine gland and was named 1656 by the anatomist Thomas Wharton from the Greek word *thureoeidés*, meaning shield-shaped. In man the thyroid gland is located anterior in the neck below the larynx, and consists of two lobes situated symmetrically and laterally on the trachea. The lobes are connected by an isthmus, on which a pyramidal lobe is sometimes found. The thyroid gland contains follicles, which could be described as convex entities, consisting of a single layer of follicle epithelial cells (thyrocytes) surrounding the follicular lumen, and an inner cavity containing colloid matter (Figure 1.1). In the space between the follicles and the parafollicular cells, C-cells, can be found, which produce the peptide hormone calcitonin. Inbetween the follicles, blood vessels and connective tissue are also located. The main function of the follicle epithelial cell is the production of the thyroid hormones triiodothyronine (T_3)

and thyroxine (T_4), which are synthesized from iodide, iodine in its ion form (I^-), and tyrosine. T_3 and T_4 are vital for cellular growth and metabolism, and calcitonin for the regulation of calcium. The colloid matter in the follicle lumen contains the protein thyroglobulin (Tg), and stores T_3 and T_4 [13].

The average weight of the euthyroid (normal thyroid) gland in mice, rats and man are approximately 3 mg [14], 30 mg [15] and 19 g [16], respectively. The size of the thyroid gland also varies depending on sex, age, diet, thyroid disorders, and during pregnancy [17]. The thyroid volume composition of colloid, follicular and stromal cells vary with age, diet and species. A crude estimate of the volume distribution for mouse, rat and man is 40-75% for the colloid, and of the residual space about 70-80% are follicle epithelial cells [17, 18].

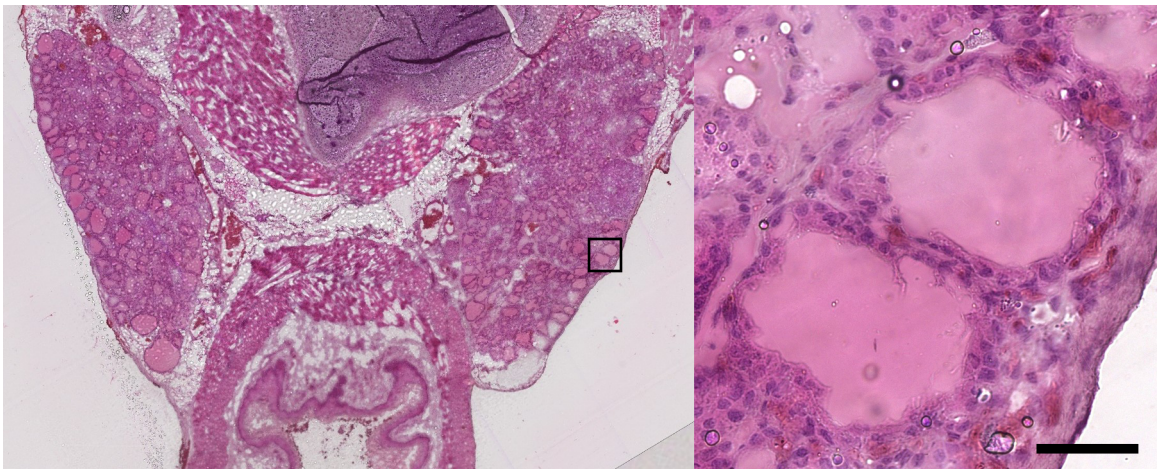

FIGURE 1.1. A 6 μm cryosection of a rat thyroid gland stained with hematoxylin and eosin. The left-hand figure shows the two thyroid lobes situated laterally. The right-hand figure shows two follicles. The bar in the right lower corner represents 50 μm.

1.1.1 Transport Of Iodide And Astatine

The follicle epithelial cells are polarized having a basolateral side facing the extra follicular area, and an apical side facing the follicle lumen. Tight junctions connect the follicle epithelial cells and prevent other transport paths of iodide other than through the follicle cells. The transport of iodide from the basolateral side into the follicle epithelial cells is mediated by the sodium iodide symporter (NIS), an intrinsic plasma membrane protein. Iodide is transported together with two sodium ions (Na^+) into the follicle epithelial cell. The iodide is translocated to the apical membrane, and the transport through the apical membrane into the follicle lumen is not fully understood but involves pendrin, a chloride-iodide transport protein [19]. Transport of free ^{211}At has not been investigated to the same extent as the transport of iodide, but observations from *in vitro* experiments showed that there were both similarities and differences in the transport, e.g. transport of both radionuclides seems to involve NIS [20].

1.1.2 Biodistribution Of Iodide And Astatine

Several biodistribution studies have been performed for radioiodide ($^{125}I^-$ and $^{131}I^-$) and free astatine (^{211}At) in the thyroid gland for different species [2, 7-12, 21-23]. Preclinical studies have shown that the uptake in the thyroid gland of radioiodide is much higher than ^{211}At, but lower in extrathyroidal tissues [7, 8, 10, 12]. The highest activity concentration (corrected for physical decay) for radioiodide ($^{125}I^-$ and $^{131}I^-$) and free ^{211}At was reported at 18-24 hours after injection in rats and guinea pigs [7, 9, 10, 24], and in mice the highest activity concentration of free ^{211}At was reported to occur about 4 hour after injection [8, 23].

Autoradiographical imaging techniques have been used to investigate the location at different time-points, as well as the transport of radiohalogens within the thyroid gland [10, 24-34]. Studies have demonstrated heterogeneity in the intrathyroidal distribution of radioiodide [24, 27-30]. Preclinical studies have shown a very fast uptake of radioiodide after administration in the thyroid gland [26, 29-31], and located within the follicle lumens within 30 seconds after injection [31]. The radioiodide appears as rings in the autoradiographical images in the peripheral region of the follicle lumen [27, 28, 30, 31]. Thereafter, the radioiodide is transported throughout the follicle lumen towards a homogenous distribution [27, 28]. The rings were more common in peripheral follicles compared to central follicles 1 hour after administration, but were less frequent at late times. However in another study peripheral rings were still observed as long as 99 days after administration [27]. Smaller follicles showed higher concentration of radioiodide at early time points, and as the equilibration process proceeded the difference in concentration became less dependent of follicle size [24, 28].

Autoradiography of ^{211}At in thyroid glands in rats has shown a higher concentration in the centrally located smaller follicles, and lower in larger follicles located peripherally [10]. Preclinical studies of ^{211}At performed on mice showed a heterogeneous distribution among the follicles, with up to a 20-fold difference between highest and lowest concentration 4 hours after injection within the thyroid gland [25].

1.2 Non-radiative Transitions

Non-radiative (NR) transitions are processes when particles are emitted from an atom at decay, e.g. Auger electrons, internal conversion electrons, and beta and alpha particles. These charged particles are directly ionising and undergo a large number of interactions with the surrounding medium. The range of these charged particles in tissue (approximated as liquid water with unit density) varies from fractions of a nanometre to centimetres (Table 1.1).

TABLE 1.1. The continuous slowing down approximation range (R_{CSDA}) for monoenergetic electrons [35, 36] and alpha particles [37] in unit density liquid water.

	Kinetic energy (keV)	Range (μm)
Electrons	1	0.061*
	10	2.5
	30	18
	50	43
	100	140
	500	1800
	1000	4400
	1500	7100
	2000	9800
	2500	12500
	3000	15000
Alpha particles	4998	38
	5138	39
	5210	40
	5867	48
	6569	57
	6891	62
	7450	70

* Range calculated using a analytical expression by Cole based on measurements [36].

1.2.1 AUGER AND INTERNAL CONVERSION ELECTRONS

Electron capture (EC) is the decay process when an unstable nucleus with an excess of protons captures an orbital electron. A proton in the nucleus is then converted to a neutron, and simultaneously emits an electron neutrino. This process creates a vacancy in the electron shell of the daughter atom, which can be filled by an electron from an outer shell, resulting in the emission of either a characteristic X-ray or an orbital electron. The emitted orbital electron is called Auger electron after Pierre Auger, a French physicist who was credited for its discovery (today it is accepted that the Austrian-Swedish physicist Lise Meitner actually discovered the effect in 1922 [38]). For each emitted Auger electron a new vacancy is created, resulting in cascades of emitted Auger electrons. The Auger effect is usually a collective name, including the Coster-Kronig and super Coster-Kronig effect, which are special cases of the Auger process [39] (Discovered by the physicists Dirk Coster and Ralph Kronig in 1935 [40]). The time frame for the Auger effect is between 10^{-16} to 10^{-14} seconds, after which the atom is in a highly charged state, and electrons from the surrounding continuum fills the vacancies neutralising the charged daughter atom [41]. The Auger, Coster-Kronig and super

Coster-Kronig electrons (AE) are monoenergetic and the number of possible initial kinetic energies can exceed a few thousands depending on radionuclide. For ^{125}I, a total number of 724 different initial kinetic energies between 0.8 eV and 31.8 keV are possible [5], with a corresponding continuous slowing down approximation range (R_{CSDA}) from a fraction of a nanometre (nm) to approximately 20 micrometres (µm) in liquid water [35] (Table 1.1). The energy deposited by electrons per unit length, the linear energy transfer (LET) (Figure 1.2a), could be as high as 26 keV/µm for low energy AE [42].

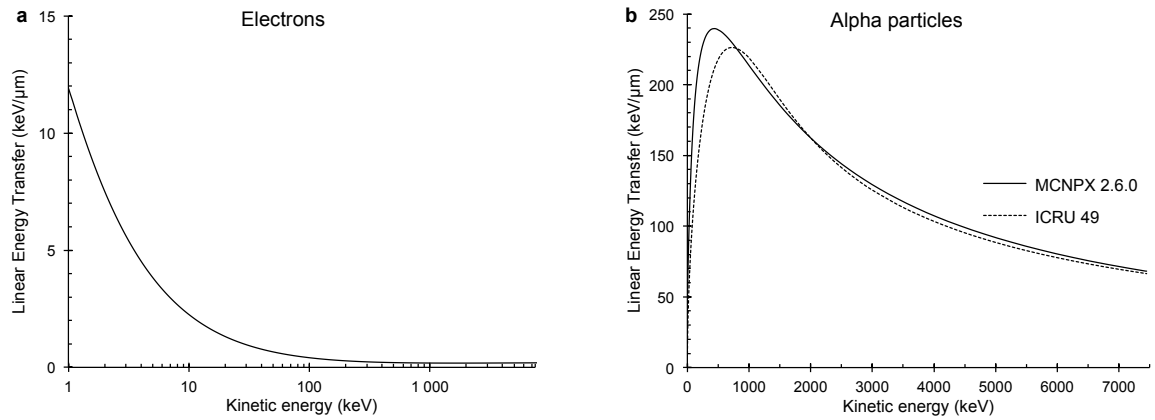

FIGURE 1.2. Linear energy transfer (LET) in liquid water as a function of kinetic energy for **a)** electrons (1-7500 keV) based on collision stopping power data from ICRU 37 [35], note the logarithmic scale on the abscissa, and **b)** alpha particles (1-7500 keV) based on collision stopping power data, the dotted line represent data from ICRU report 49 [37], and the filled line data from Janni et al., scaled from protons [43], and used in the Monte Carlo code MCNPX 2.6.0. Note the different scales on the ordinates.

Internal conversion (IC) is a process when a nucleus in an atom with an excess of energy de-excites, and energy is transferred to an orbital electron and is emitted from the atom. This is a competing process with the emission of a γ-ray. The emitted orbital electron in the IC process is called internal conversion electron (CE), and usually has a higher initial monoenergetic energy than AE, e.g. for ^{123}I with initial kinetic energies between 127 keV and 1068 keV [5], and with a corresponding R_{CSDA} from about 0.2 mm to 4.7 mm in liquid water [35]. LET for high energetic electrons is low, about 0.2 keV/µm, for the most of their long range in a medium [42] (Figure 1.2). The emitted CE creates a vacancy in one of the electron shells, which can be filled by an electron from an outer shell and the difference in energy can be released as either a characteristic X-ray or an orbital electron, similar to the previously described EC decay, and could lead to a cascade of emitted AEs.

1.2.2 Beta Particles

The beta decay (β decay) is a process in which the nucleus can correct for an excess of protons or neutrons. When there is an excess of neutrons an electron (β^- particle) is

emitted from the nucleus, and conversely a positron (β^+ particle) when there is an excess of protons. The β^+ particle has the electric charge +1 and the β^- particle -1, and the particles are each other's antiparticles. In the β decays the emitted β particles shares the kinetic energy with an electron neutrino (β^+ decay), or an electron antineutrino (β^- decay), which results in continuous β energy spectrums (Figure 1.3). The recoil energy of the daughter nucleus is in the order of 10-100 eV [39].

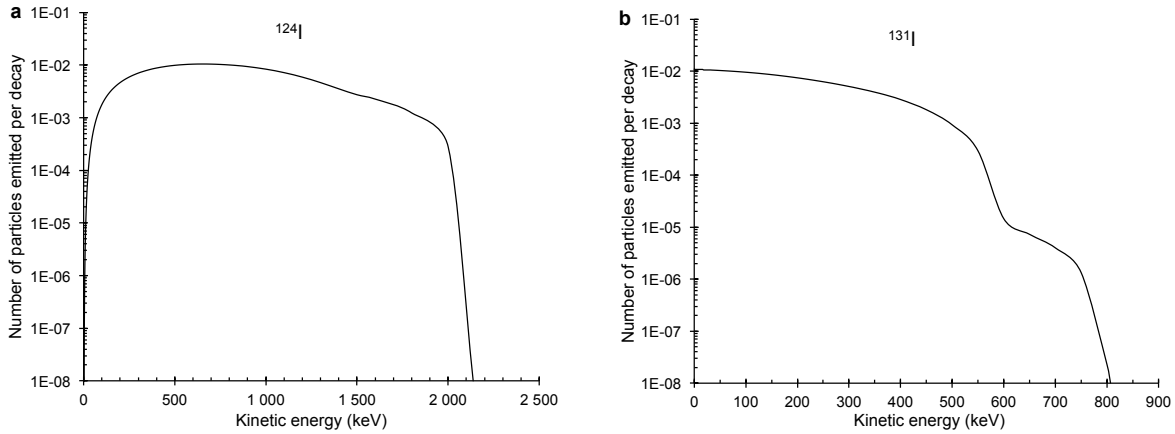

FIGURE 1.3. The full β particle energy spectrum from ICRP 107 [5] for **a)** ^{124}I with an endpoint energy of 2138 keV and the average β^+ particle energy of 187 keV per decay, and for **b)** ^{131}I with an endpoint energy of 807 keV and the average β^- particle energy of 183 keV per decay. Note the logarithmic scale on the ordinates (Figure 1, Paper I).

1.2.3 Alpha Particles

The alpha particle decay (α decay) is a process when the unstable atomic nucleus emits an alpha particle (α particle). The α particle is a helium nucleus (^{4}He), which consists of two protons and two neutrons, and has the electric charge +2. About 98% of the kinetic energy released in the decay (Q value) are carried away by the α particle, and about 2% remain as recoil energy to the daughter nucleus [44], e.g. for ^{211}At the kinetic energy of the emitted main α particle is 5.87 MeV, and the recoil energy of the daughter nucleus ^{207}Bi is 114 keV [45]. The α particle has a high LET, varying approximately between 60 and 240 keV/μm in liquid water (Figure 1.2b) [37].

1.3 Radiohalogens

According to the International Union of Pure and Applied Chemistry (IUPAC) the halogens are situated in nomenclature group 17, which consists of 5 elements, and two of the elements are iodine (I) with atomic number 53, and astatine (At) with the atomic number 85. Iodine from the Greek word *ioeides*, meaning violet or purple has 37

isotopes ranging from ^{108}I to ^{144}I, with only one stable isotope (^{127}I) [46]. Astatine from the Greek word *astatos*, meaning unstable, has 32 isotopes ^{191}At and ^{193}At to ^{223}At, with no stable isotopes [46]. The nuclear decay data used in this work was from the International Commission on Radiological Protection (ICRP) publication 107 [5], which 2009 superseded the ICRP publication 38 [47].

TABLE 1.2. Nuclear decay data from ICRP 107 [5] for ^{123}I, ^{124}I, ^{125}I, ^{131}I, ^{211}At and their respective daughter atoms including, decay mode, yield, physical half-life, photon-to-electron energy ratio (p/e)*, average number of AE emitted per decay, and the number of possible CE energies per decay (Table 1, Paper I).

Radionuclide / Daughter nuclides	Decay mode	Yield	Half-life	p/e*	AE per decay	CE energies per decay
^{123}I /	EC	1.0	13 h	6.1	14	246
^{123}Te	EC	9.9996E-01	6.0E+14 y	0.14	9.7	-
^{123m}Te	IT	4.4E-05	119 d	1.5	13	17
^{124}I	EC	0.77	4.2 d	5.7	9.2	358
	β^+	0.23				
^{125}I	EC	1.0	59.4 d	2.2	23	6
^{131}I /	β^-	1.0	8.0 d	2.0	0.7	108
^{131m}Xe	IT	1.2E-02	12 d	0.14	11	6
^{211}At /	EC, α	0.58, 0.42	7.2 h	6.2	6.5	18
^{211}Po	α	1.0	0.52 s	41	0.03	18
^{207}Bi	EC, β^+	1.0	33 y	13	13	36

* Defined as the total energy emitted as photons divided by total energy emitted as electrons [48].

1.3.1 Radioiodine (^{123}I, ^{124}I, ^{125}I and ^{131}I)

^{123}I (half-life 13 hours) decays by EC directly or via ^{123m}Te to ^{123}Te. ^{123}Te decays by EC to stable ^{123}Sb, but could for practical reasons be considered as stable due to the very long half-life of $6.0 \cdot 10^{14}$ years (Figure 1.4). ^{123}I emits on average 14 AEs per decay, this due to after the EC decay the ^{123}Te daughter nucleus remains in an excited state, and the yield of emitting a γ-ray is 84% compared with 16% for a CE. The number of possible initial kinetic energies for the CE is 246. Of the total energy emitted per nuclear transformation 14% is from electrons and 86% from photons, with a photon-to-electron energy ratio of 6.1 (Table 1.2) [5].

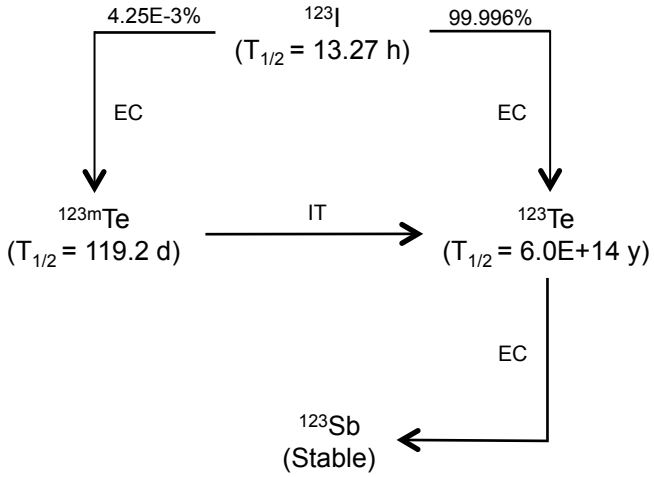

FIGURE 1.4. Simplified decay scheme of ^{123}I [5].

^{124}I (half-life 4.2 days) decays by EC or by emitting a β^+ particle to stable ^{124}Te (Figure 1.5). ^{124}I emits on average 9.2 AEs per decay, and the β^+ particle energy spectrum, including all four independent spectra with an endpoint energy of 2138 keV, and average energy of 187 keV per decay (Figure 1.3a). The number of possible initial kinetic energies for the CE is 358. Of the total energy emitted per nuclear transformation 15% is from electrons and 85% from photons, with a photon-to-electron energy ratio of 5.7 (Table 1.2) [5].

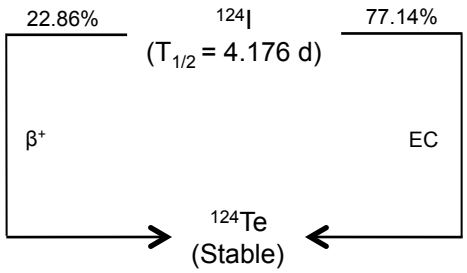

FIGURE 1.5. Simplified decay scheme of ^{124}I [5].

^{125}I (half-life 59 days) decays by EC to ^{125}Te (Figure 1.6). ^{125}I emits on average 23 AEs per decay, since after the EC decay the ^{125}Te daughter nucleus is in an excited state, and the yield of emitting a γ-ray is 5.5% compared with 94.5% for emitting a CE. This results in a high possibility of two cascades of AEs and hence the large number of AEs emitted per decay. The number of possible initial kinetic energies for the CE is 6. Of the total energy emitted per nuclear transformation 31% is from electrons and 69% from photons, with a photon-to-electron energy ratio of 2.2 (Table 1.2) [5].

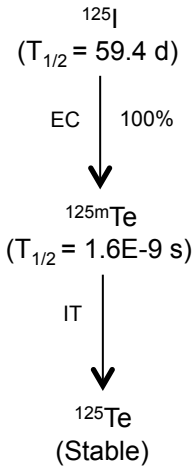

FIGURE 1.6. Simplified decay scheme for ^{125}I [5].

^{131}I (half-life 8.0 days) decays by emitting a β^- particle directly to stable ^{131}Xe, or via ^{131m}Xe (Figure 1.7). ^{131}I emits on average 0.7 AEs per decay, and the β^- particle energy spectrum, including all six independent spectra, with an endpoint energy of 807 keV, and the average energy of 183 keV per decay (Figure 1.3b). The number of possible initial kinetic energies for the CE is 108. Of the total energy emitted per nuclear transformation 33% is from electrons and 67% from photons, resulting in a photon-to-electron energy ratio of 2.0. ^{131m}Xe with a half-life of 12 days decays to ^{131}Xe, and emits on average 11 AEs per decay, and the number of possible initial kinetic energies of the CE is 6 (Table 1.2) [5].

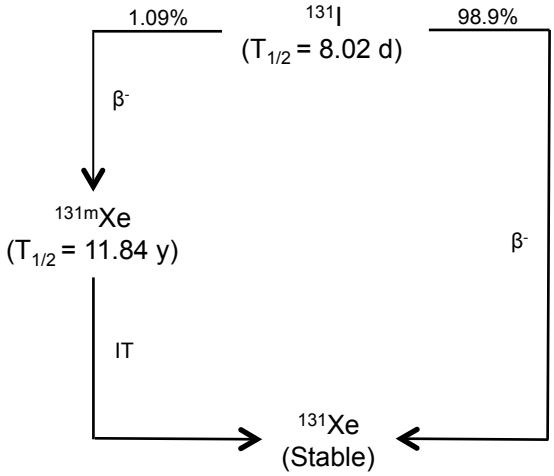

FIGURE 1.7. Simplified decay scheme for ^{131}I [5].

1.3.2 Astatine (^{211}At)

^{211}At was first produced 1940 at the University of California in Berkley, USA, by Corson et al. and was called element 85 [49] or eka-iodine, and in 1947 it was given the name astatine [50]. ^{211}At (half-life 7.2 hours) decays via a double-branched pathway both by emitting a α particle to stable ^{207}Pb (Figure 1.8). There are seven possible initial kinetic energies for the emitted α particle, and the two main are 5.867 MeV and 7.450 MeV. The daughter nuclide ^{207}Bi has a half-life of 33 years and its contribution is usually excluded in dosimetric studies, due to long half-life and the lack of α particle emission at decay. In the ^{211}At decay on average 6.5 AEs are emitted, and the number of possible initial kinetic energies of the CE is 18 (excluding ^{207}Bi) (Table 1.2) [5].

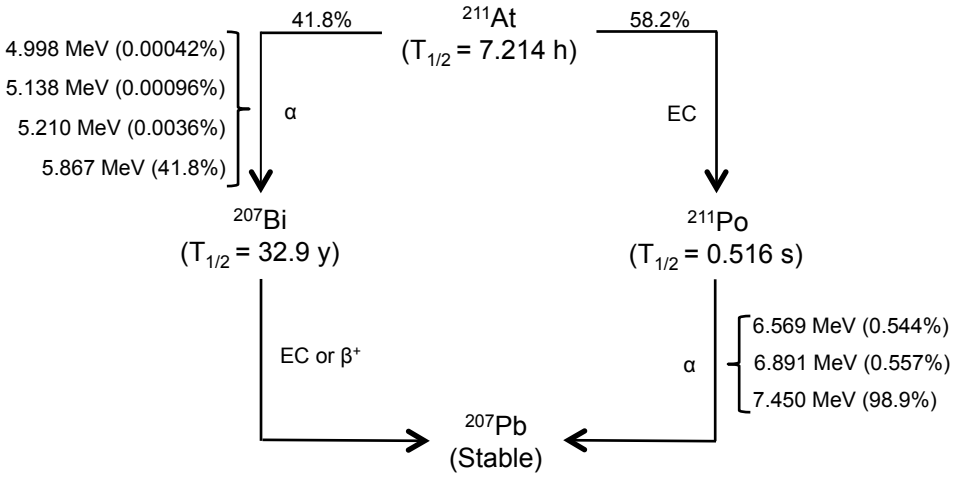

FIGURE 1.8. Simplified decay scheme for ^{211}At [5].

1.3.3 Medical Applications

There are several areas of use in nuclear medicine for the radiohalogens ^{123}I, ^{124}I, ^{125}I, ^{131}I and ^{211}At, and below are some examples of applications listed and described.

^{123}I has a relatively short half-life and emits photons suitable for scintigraphy. In treatment of thyroid cancer with ^{131}I (as iodide), ^{123}I (as iodide) scintigraphy has been used for dose planning [51]. Similarily, scintigraphy using the norepinephrine analogue meta-iodobenzylguanidine (MIGB) labelled with ^{123}I (^{123}I-MIBG) is performed for planning therapy of malignant pheochromocytomas using ^{131}I-MIBG [^{123}I]FP-CIT (Ioflupane, DaTscan™) SPECT imaging of the brain is used for diagnosis of parkinsonian syndromes [52].

Due to the emitted positrons ^{124}I can be used for diagnostic imaging using positron emission tomography (PET). ^{124}I has a long half-life compared with most of the positron emitters routinely used today, making it interesting for studies concerning tissue

residence and metabolization of radioiodinated molecules [53]. In differentiated thyroid cancer ^{124}I-PET/CT based dosimetry may contribute to a more accurate administered therapeutic activity of ^{131}I [54].

^{125}I emits photons with energies not suitable for gamma camera scintigraphy, but can be used with other types of detectors. ^{125}I labelled methylene blue (^{125}I-MB) has recently been used in a phase II trial for sentinel lymph node identification in women with breast cancer, with promising results [55].

^{131}I emits photons that can be used for scintigraphy but is mainly used for therapy with due to the high-energy β^- particles emitted, especially for hyperthyroidism and metastatic thyroid carcinoma [51]. As described above, ^{131}I-MIBG is used for treatment of pheochromocytoma and ^{131}I bound to a chimeric monoclonal antibody (^{131}I-tositumomab, Bexxar®) is used for dose planning and therapy on patients with B-cell non-Hodgkin lymphoma (NHL) [56].

There is an increasing interest of using α particle emitters in cancer therapy. A few clinical trials have investigated the therapeutic potential of ^{211}At. Treatment with a chimeric antitenascin monoclonal antibody 81C6 labelled with ^{211}At (^{211}At-ch81C6) of patients with recurrent central nervous system tumours has shown promising results [3]. A phase I study involving the treatment of microscopic ovarian cancer with a monoclonal antibody fragment labelled with ^{211}At (^{211}At-MX35 F(ab')$_2$) showed promising results [4].

1.4 Internal Dosimetry

The absorbed dose, D, is a non-stochastic quantity and is defined by the International Commission on Radiation Units and Measurements (ICRU) report 85 [57] as

$$D = \frac{d\bar{\epsilon}}{dm}, [Gy],$$

where $d\bar{\epsilon}$ is the mean energy imparted by ionising radiation to matter of mass dm and is expressed in the unit J/kg or Gy.

1.4.1 MIRD Formalism

The MIRD (Medical Internal Radiation Dose) formalism is a framework for assessment of the absorbed dose from internally administrated radionuclides for e.g., whole organ, part of a tissue, voxelized tissue structures or individual cellular compartments in diagnostics or therapy [58, 59]. In 2009 the MIRD Pamphlet No. 21 was published, with the purpose of standardising the nomenclature between the MIRD and ICRP systems

[60]. The MIRD formalism assumes a homogenous distribution of the radionuclides within the respective source region, and also that the atomic and mass density composition of the medium is homogeneous in both the source and target regions.

The absorbed dose, $D(r_T)$, in the target region, r_T, is calculated according to

$$D(r_T) = \tilde{A}(r_S) \cdot S(r_T \leftarrow r_S)\ , [Gy],$$

where $\tilde{A}(r_S)$ is the time-integrated activity (total number of nuclear transformations) in the source region, r_S. The S value, $S(r_T \leftarrow r_S)$, is the mean absorbed dose in r_T per nuclear transformation in r_S.

The S value can also be expressed as

$$S(r_T \leftarrow r_S) = \frac{\phi(r_T \leftarrow r_S) \cdot E}{M(r_T)}\ , [Gy/Bq \cdot s],$$

where $\phi(r_T \leftarrow r_S)$ is the absorbed fraction in r_T of the energy emitted per nuclear transformation, E, from r_S, and $M(r_T)$ is the mass of r_T.

The S value can be calculated using analytical, e.g. [59, 61-64] or Monte Carlo methods, e.g. [65, 66], and the choice of method depends on e.g., the complexity of the geometry, different atomic and density compositions, and the spatial distribution of the radionuclide. In some situations the S-value should not be treated as a constant value e.g., when calculating the absorbed dose to a tumour that changes in size during the time of exposure [67]. S values could also be calculated for different source compartments to investigate the self-dose ($r_T = r_S$) and the cross-dose ($r_T \neq r_S$).

The time-integrated activity $\tilde{A}(r_S)$, which in the MIRD primer [58] was called the cumulated activity, is the total number of decays that occurs within the source region. $\tilde{A}(r_S)$ can be determined with quantitative imaging (e.g. PET, SPECT or planar scintigraphy) at different time-points after administration, to obtain the activity of the radionuclide in the source region as a function of time, $A(r_S, t)$. Usually the time period ranges from the time of administration at ($t = 0$) to infinity ($t = \infty$), and the area under the time-activity curve is $\tilde{A}(r_S)$.

$$\tilde{A}(r_S) = \int_0^\infty A(r_S, t)\, dt\ , [Bq \cdot s].$$

Other methods include determination of activity concentration in tissue samples connected to a kinetic model (e.g., blood, urine or tissue biopsies). Compartment modelling could also be used to predict the activity in a tissue of interest if no measured data are available or possible to obtain.

The MIRD-formalism was used in this work (Papers II and III) for specified source and target regions to calculate the mean absorbed dose.

1.4.2 MICRODOSIMETRY

A medium consists of atoms with which the ionising radiation interacts and deposits energy in discrete stochastic steps. When the volume of the medium is reduced the fluctuation of the energy density induced by the ionising radiation increases. For small volumes the variation in energy density could be very large, fluctuating from zero (no energy deposited within the volume) to very high values (order of several Gy). These stochastic fluctuations are the consequence of several factors, e.g. size of the volume, finite range of the particle, LET, generation of δ-particles, energy loss straggling, and the number of particles that crosses the volume [68]. For α particles (high LET) that cross through a cell nucleus the effect can be so high that the mean absorbed dose can be misleading as an index for the biological effect [69]. The energy deposited by α particles that traverse the cell nucleus will give rise to statistical variations. These variations depend on the number of α particles that traverse the cell nucleus, the path-length through the cell nucleus, the kinetic energy of the α particle when it crosses through the cell nucleus, i.e. LET (Figure 1.2b). This is important for low absorbed doses when few α particles traverse the cell nucleus.

The concept of microdosimetry was originally proposed by Rossi, and includes a conceptual framework and stochastic quantities (describe the stochastic nature of energy deposition of ionising radiation in a medium) to help interpreting radiation effects, which could not be explained with macrodosimetry [70].

There are four basic stochastic quantities defined, which are described in more detail in the ICRU report 36 [71]: energy deposit, ϵ_i (J or eV), energy imparted, ϵ (J or eV), specific energy, z (J/kg or Gy), and lineal energy, y (J/m or keV/µm), which all are linked.

The elementary quantity in microdosimetry is ϵ_i, which is the energy deposited in a single interaction, i, and is defined as

$$\epsilon_i = T_{in} - T_{out} + Q_{\Delta m}\ , [J],$$

where T_{in} is the energy of the incident ionising particle and T_{out} is the sum of the energies of all ionising particles leaving the interaction. $Q_{\Delta m}$ is the change in rest mass energy of all particles involved in the interaction, including the atom [71].

ϵ is the energy imparted to matter in a volume and is defined as

$$\epsilon = \sum_i \epsilon_i\ , [J].$$

z in units of Gy is the stochastic analogue to the absorbed dose, and is defined as ϵ in a specific volume divided with the mass, m, of the volume in units of kg [71].

y is the lineal energy and is defined as

$$y = \frac{\epsilon}{\bar{l}}\,, [J/m],$$

where $\bar{l}$ is the mean chord length in the volume in units of meters [71]. For a sphere the mean chord length, $\bar{l}$, is calculated according to Cauchy's theorem

$$\bar{l} = \frac{2 \cdot d}{3}, [m],$$

where d is the diameter of the sphere [72].

The calculations for particles that traverse a volume of interest will result in a distribution of z. The probability density function, $f(z)$, includes the probability of zero specific energy.

The mean specific energy, $\langle z \rangle$, includes the discrete value of $z = 0$, and is a non-stochastic quantity [71]. $\langle z \rangle$ could also be used as an alternative definition for the absorbed dose

$$D = \lim_{m \to 0} \langle z \rangle\,, [Gy],$$

where D is equal to the limit of $\langle z \rangle$ when the mass, m, approaches zero, and the mean absorbed dose, $\overline{D}$, is equal to $\langle z \rangle$ in that volume [57].

In most cases the discrete component of zero z will dominate, unless the target and source compartment of the emitted particles are the same. To investigate the distribution of z for charged particles that transverses the volume of interest and deposits energy ($z > 0$) the probability density function, $f(z_1)$, called the single-hit specific energy distribution can be used. The corresponding mean value for this distribution is $\langle z_1 \rangle$, which is called the single-hit mean specific energy per event, and is a non-stochastic quantity. The lineal energy distribution, $f(y)$, is only defined for single energy deposition events, and the corresponding mean value for this distribution is $\langle y_F \rangle$, which is called the frequency mean lineal energy, and is a non-stochastic quantity [71].

1.5 The Monte Carlo Method

The Monte Carlo (MC) technique is a statistical method employing random numbers to simulate stochastic processes, and was named by Nicholas Metropolis after the Monte Carlo casino in Monaco [73]. The MC method is excellent for simulation of the stochastic nature of ionising radiation, and its interaction with matter (radiation transport). The earliest documented use of random numbers was a method by Comte de Buffon in 1777, when needles were tossed on a table with parallel lines from which the value of π could

be determined [74]. The real start in modern times for MC technique was during World War II, when scientists used MC methods in the Manhattan project to develop the atomic bomb. The possibility of exploring the full potential of the MC technique started with the digital computer.

When performing MC calculations probability density functions (PDFs) are used, which describes different physical processes, e.g. angular scattering cross sections. To sample data from PDFs a pseudo-random number generator (PRNG) is used, which through an algorithm generate random numbers. The random numbers is used to sample the location, direction and initial kinetic energy of the emitted particles. An example of a PRNG is the linear congruential random number generator (LCGRNG), which is an algorithm that uses a linear equation to yield a sequence of random numbers [73].

Several general-purpose radiation transport MC codes exist that can be used for dosimetric calculations. In the present work the MC code MCNPX 2.6.0 (Monte Carlo N-Particle eXtended) was used, developed at Los Alamos National Laboratory, USA [75]. Recently a production version of the MC code MCNP6 (Monte Carlo N-Particle) was released, which is a fusion (including new features) between the MC codes MCNP5 and MCNPX. The new MCNP6 code includes transport of photons, neutrons, electrons, heavy charged particles and has extended the energy cut-off for electrons and photons down to 10 eV and 1 eV, respectively [76]. The Electron Gamma Shower (EGSnrc) MC code from the National Research Council in Ottawa (Canada), which is a general purpose MC code for coupled electron-photon transport for particle energies down to 1 keV [77, 78]. PENELOPE-2011 (PENetration and Energy Loss of Positrons and Electrons) is a coupled electron-photon general MC transport code developed in Spain [79]. GEANT4 (GEometry ANd Tracking) is a toolkit for radiation transport for photons and a wide range of charged particles developed at Organisation Européenne pour la Recherche Nucléaire (CERN) [80].

1.5.1 THE MCNPX CODE

Monte Carlo N-Particle eXtended (MCNPX) is a general-purpose radiation transport code. The MCNPX program began 1994 as an extension of MCNP4B, which had neutron, photon and electron capabilities. The MCNPX 2.6.0 MC code was released in 2008, and was used in this work mainly due to *1)* the capability of simulating electrons, positrons and α particles, *2)* the code started being developed in 1963 and have been thoroughly tested and evaluated during the years of use, *3)* the MCNPX MC code uses input files for which no major programming knowledge is needed. (The structure of input files originates from the time of the computers that used punch cards as input.) The first block in the input file contains the cell card, which defines the geometric volumes, with respective materials and densities. The second block is the surface card containing the geometric surfaces from which the volumes are created. The third block is the data card and contains the physics and source cards, which in short defines the material, source

geometry, particle type, kinetic energy, energy cut-off, direction of emitted particle, tallies, and other characteristics [75]. There are two interactive graphical user interfaces available for aid in the design of the geometry and problem setup, Visual editor [81] and MORITZ [82]. The tally is a user-defined detector, e.g. volumes or surfaces, which scores data used in the calculations. To investigate the energy deposited in a predefined volume the tallies *F8 in units of MeV, or F6 in units of MeV/g can be used, and F8 for the energy distribution in MeV of pulses created in the volume. In electron transport the F6 tally is only valid when the electrons are confined in the cells where they are created, and for electron transport *F8 tally is preferred since all details in the transport are followed. Tally F6 can be used for α particle transport, using only continuous slowing down energy loss, not accounting for δ-particles or bremsstrahlung.

The transport calculations of α particles in the MC code MCNPX uses the collision stopping power data for energy loss from protons, which are scaled to α particles [43]. For the α particles in the MC code MCNPX small angle Coulomb scattering is accounted for using Rossi-Griesen algorithm and Vavilov logic for energy straggling [83].

For electron and positron calculations identical particle transport physics are used, the difference is that the positron annihilates at the end of its track and creates two 511 keV photons, which are emitted in the opposite direction of each other. The stopping power data for electrons from ICRU report 37 are used for positrons and electrons. The total stopping power values in ICRU report 37 are slightly higher for positrons at lower kinetic energies (<35 keV), and slightly lower for higher kinetic energies compared with electrons [35]. As previously mentioned the number of Coulomb interactions that an electron undergoes through its path through a medium is very large, and to simulate each individual interaction would result in very long simulation times. A method called multiple scattering or condensed histories was proposed in 1963 by Berger [84]. This method proposes two different simulation strategies for electron transport, Class I and Class II. Class I uses predetermined sets of path lengths or energy losses, which include both inelastic and elastic interactions. Class II simulates the inelastic interactions individually, and the elastic interactions are described collectively. In MCNPX the transport of electrons is a mixture of condensed history (Class I) and single interactions (Class II) of so-called catastrophic events. The MC code MCNPX uses condensed history for collisional energy loss and individual simulated interactions for, e.g. radiative loss.

The MC code MCNPX has standard predefined energy steps, i, as a function of the kinetic energy, E_i. This is the representation of a logarithmic energy grid where 8 steps equal a factor of 2 in energy.

$$\frac{E_{i+1}}{E_i} = \left(\frac{1}{2}\right)^{1/8} = 0.917$$

Each standard energy step represents an average kinetic energy loss of 8.3%, and each respective energy step is divided into angular and energy substeps. The default number

of substeps is dependent on the material (average atomic number) used in the simulations, the larger average atomic number the more substeps. For liquid water the default number of substeps is 3, which could be changed by the user, but more substeps results in longer simulation times. The collision energy loss is calculated at the energy step level from the Continuous Slowing Down Approximation (CSDA) using Landau [85] and Bluck-Leisegang [86] theories for energy straggling. At the substep level angular deflections using the Goudsmit-Sanderson theory [87], and the generation of δ-particles are sampled.

The MC code MCNPX uses a LCGRNG for the creation of random numbers using 48-bit integers as default, which has a period of $2^{46} \approx 7 \cdot 10^{13}$, and could be extended to 63-bit integers. The MCNPX MC code performs 10 statistical checks to validate the generated results, which include the relative error (R). The relative error is equal to $S_{\bar{x}}/\bar{x}$, where $S_{\bar{x}}$ is the estimated standard deviation and $\bar{x}$ the estimated mean [88].

To improve the statistics in MC calculations there are two strategies that can be used: *1)* to increase the number of simulated histories, or *2)* to use variance reduction methods. The number of histories simulated, N, is linearly proportional to the simulation time, T, and R is proportional to $1/\sqrt{T}$, e.g., if a 2-hour simulation gives a R of 0.1, it will take 200 hours to achieve a R of 0.01. Variance reduction techniques can be used to reduce the relative error with equal simulation time. Examples of basic variance reduction are *1)* the use of energy cut-off, if the simulate particles energy is lower than a predefined energy the history is terminated, and *2)* defining the geometry in a way that when particles are not contributing to the results the history is terminated.

2. AIMS

The aims of this work were to:

- Calculate mean specific energy, ⟨z⟩, per decay (S value) for the NR transitions of ^{123}I, ^{124}I, ^{125}I, ^{131}I and ^{211}At homogeneously distributed in unit density spheres of different sizes, using the MC code MCNPX and recent nuclear decay data from ICRP (Paper I). The following issues were also studied:
    - the relative contributions to ⟨z⟩ per decay from AE, CE, and β and α particles
    - the difference in ⟨z⟩ per decay when the full β particle energy spectrum and the average β particle energy is used for ^{124}I and ^{131}I
    - the difference in ⟨z⟩ per decay when using data for all NR transitions for ^{211}At compared with using the average α particle energy

- Develop species-specific thyroid follicle models for man, rat and mouse (Papers II and III)

- Study the effect of geometry, distribution and concentration for ^{123}I, ^{125}I, ^{131}I and ^{211}At in the developed species-specific thyroid follicle models (Papers II and III)

3. METHODS

3.1 MATHEMATICAL MODELS

3.1.1 WATER SPHERES

The mathematical models used in Paper I were spheres with diameters from 1 µm to 1 cm centrally placed within a 10 cm sphere. The model consisted of liquid water with unit density (1.0 g/cm^3). The source and target volumes were the same, and the radiohalogens were homogenously distributed within the spheres.

3.1.2 SINGLE THYROID FOLLICLE MODELS

The species-specific single thyroid follicle models for man, rat and mouse (Papers II and III) consisted of a centrally place follicle lumen represented by a sphere. A single layer of follicle cells represented by a concentric spherical shell surrounded the follicle lumen. Six follicle cell nuclei were centrally placed within the follicle cells, symmetrically located on the Cartesian x, y and z-axis (Figure 3.1).

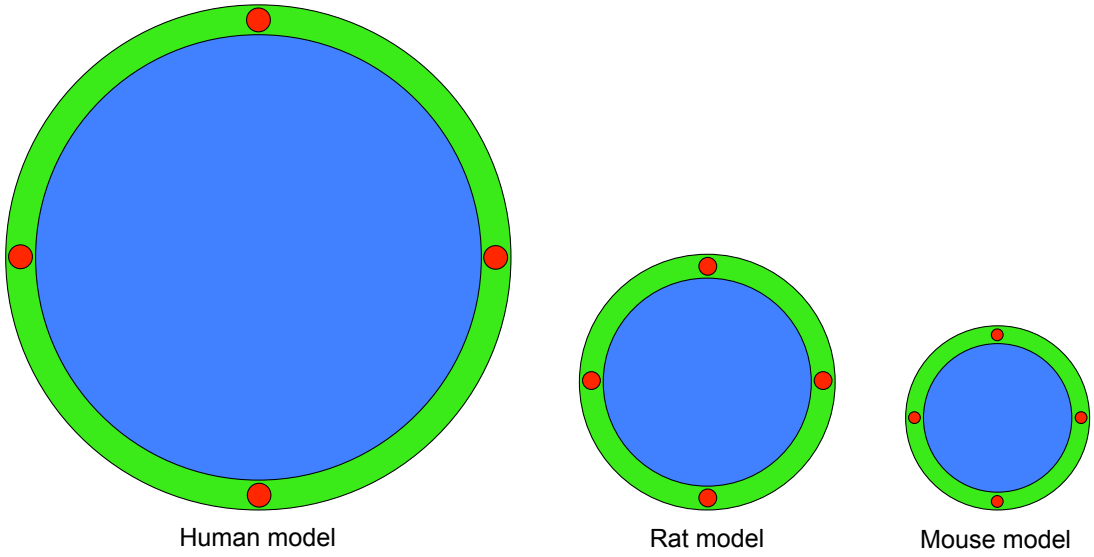

FIGURE 3.1. Schematic figures of the species-specific single follicle models of man, rat and mouse with a centrally placed follicle lumen (blue), surrounded by a single layer of follicle epithelial cells (green) with centrally placed follicle cell nuclei (red) on the Cartesian x, y and z-axes. This is a cross section through the centre of the follicle, only showing 4 of the 6 follicle cell nuclei.

The follicle cell nuclei were the target volumes and an average value was calculated for the six nuclei. The dimensions of the species-specific single follicle models of man, rat and mouse were: follicle lumen diameters 150, 70 and 50 µm; follicle cell thickness 10, 8, and 6 µm; follicle cell nucleus diameter 8, 6 and 4 µm, respectively. The models consisted of unit density liquid water (Papers II and III), and calculations were performed with 1% and 2% of organic iodine (^{127}I, density 4.94 g/cm^3) homogeneously distributed within the follicle lumen (Paper II). Species-specific models with a follicle lumen diameter varied between 10 and 500 µm in man, and between 10 and 300 µm in mouse and rat. The radiohalogens were homogenously distributed *1)* within the follicle lumen, *2)* follicle cells, *3)* the follicle cell nuclei, and *4)* homogenously distributed on concentric spherical surfaces, and in all the calculations the follicle cell nuclei were the targets.

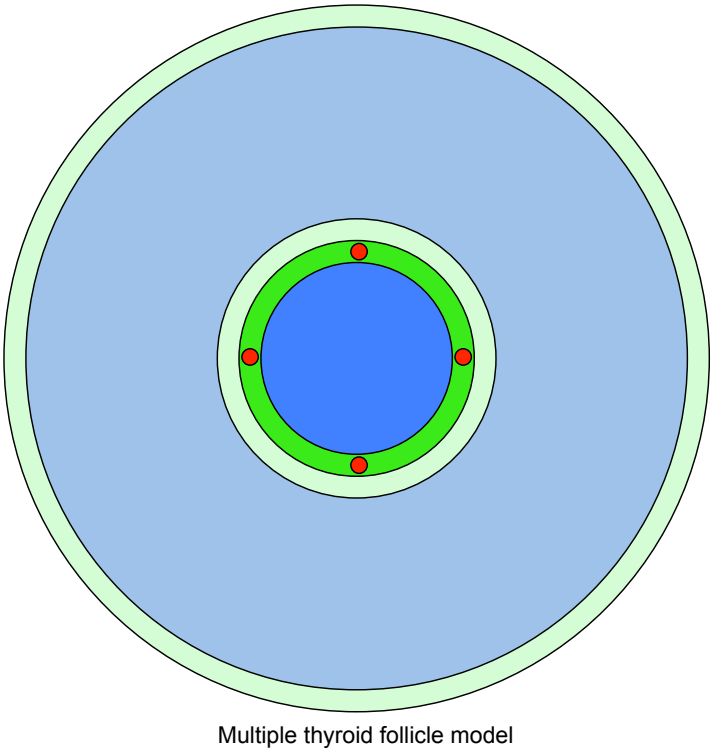

FIGURE 3.2. Schematic figure of a species-specific multiple follicle model, consisting of a central placed single follicle surrounded by a single layer of follicle epithelial cells (light green), follicle lumen (light blue), and a single layer of follicle cells (light green) representing the first surrounding layer of neighbouring follicles. This is a cross section through the centre of the multiple follicle models, only displaying 4 of the 6 follicle cell nuclei (Figure 2, Paper II).

3.1.3 Multiple Thyroid Follicle Models

The species-specific multiple follicle model for man, rat and mouse (Papers II and III) to investigate the contribution from surrounding follicles consisted of a centrally placed single follicle model, which are surrounded with neighbouring follicles. The

neighbouring follicles consisted of concentric spherical shells, representing the different layers of follicles (Figure 3.2). The thickness of the surrounding follicle lumens were for the species-specific models of man, rat and mouse 150, 70 and 50 μm, and the follicle cell thickness 10, 8 and 6 μm, respectively. The number of surrounding follicle layers contributing depends on species and radiohalogen, e.g. in the model of man the number of contributing surrounding layers were 2, 1, 8 and 1 for ^{123}I, ^{125}I, ^{131}I and ^{211}At, respectively (Table 3.1). The radiohalogens were homogenously distributed within *1)* the follicle lumen, and/or *2)* the follicle cells, and the targets were the centrally placed single follicle cells nuclei.

TABLE 3.1. The diameter of one thyroid lobe in the species-specific models of mouse, rat and man, assuming spherical geometry, only containing follicles (no interstitial tissue), and the number of contributing surrounding thyroid follicle layers for ^{123}I, ^{125}I, ^{131}I and ^{211}At in the multiple thyroid follicle models of mouse, rat and man.

		Number of contributing surrounding follicle layers			
Model	Thyroid lobe diameter (mm)	^{123}I	^{125}I	^{131}I	^{211}At
Mouse	1.4	5	1	10	1
Rat	3	4	1	16	1
Man	25	2	1	8*	1

* Follicles beyond the 8th layer contribute to less than 1% of the absorbed dose.

Approximately 80-95% of the tissue in the thyroid gland consists of follicles [18, 89]. The weight of the thyroid gland is species-specific, and the average weight of the thyroid gland is approximately 3 mg, 30 mg and 19 g for mouse, rat and man [14-16]. Assuming that 88% of the thyroid tissue consists of follicles, and the two thyroid lobes are spheres consisting of only follicles (no interfollicular tissue) of unit density (1.0 g/cm^3). Based on these assumptions the calculated diameter of the thyroid lobes in the models of mouse, rat and man were 1.4, 3 and 25 mm, respectively (Table 3.1).

3.2 Radionuclides Studied

The radiohalogens studied were ^{124}I (Paper I), ^{123}I, ^{125}I, ^{131}I (Papers I and III) and ^{211}At (Papers I and II). The nuclear decay data used in all the MC calculations was taken from ICRP 107 [5]. In the calculations for the AE conventional spectra from ICRP 107 were used, consisting of 13 composite groups for the radioiodine isotopes (Table 3.2). Nuclear decay data from MIRD for the radiohalogens were obtained from the webpage at the National Nuclear Data Centre (NNDC) at Brookhaven National Laboratory (BNL) [90].

In Paper I, the contribution from the daughter atom ^{131m}Xe in the ^{131}I decay were studied. For ^{123}I the contribution from ^{123m}Te was neglected in the dosimetric calculations due to the low yield of $4.4 \cdot 10^{-5}$, and ^{123}Te was considered stable due to the very long half-life of $6.0 \cdot 10^{14}$ year. For ^{211}At all seven possible α particles emitted were considered from the ^{211}At and ^{211}Po decays, and the contribution from the AE and CE were included. The contribution from ^{207}Bi was not considered due to the long half-life of 33 year. Calculations performed using the complete β particle energy spectrum for ^{124}I and ^{131}I was compared with calculations using the average β particle energy. AE with initial kinetic energies <1 keV were assumed to be deposited all their kinetic energy within the source compartment.

TABLE 3.2. The conventional spectra in ICRP 107 of the Auger, Coster-Kronig and super Coster-Kronig electrons for ^{123}I, ^{124}I, ^{125}I and ^{131}I with their respective yield and initial kinetic energy. K, L, M and N represent the K-shell, L-shell, M-shell and N-shell, respectively. X and Y represent vacancies in a different shell than indicated by the previous letter, e.g. AE KLX is a K-shell Auger transition where one of the two new vacancies is in the L-shell, and CK NNX represents all N-shell CK transitions [5].

	^{123}I		^{124}I		^{125}I		^{131}I	
Notation	Yield	Energy (MeV)	Yield	Energy (MeV)	Yield	Energy (MeV)	Yield	Energy (MeV)
AE KLL	8.07E-02	2.27E-02	5.39E-02	2.27E-02	1.31E-01	2.27E-02	3.94E-03	2.45E-02
AE KLX	3.56E-02	2.65E-02	2.37E-02	2.65E-02	5.77E-02	2.65E-02	1.76E-03	2.87E-02
AE KXY	3.74E-03	3.04E-02	2.50E-03	3.03E-02	6.08E-03	3.03E-02	1.89E-04	3.29E-02
CK LLX	1.56E-01	2.96E-04	1,04E-01	2,96E-04	2.76E-01	3.00E-04	8.29E-03	3.18E-04
AE LMM	7.34E-01	3.09E-03	4.91E-01	3.08E-03	1.23E+00	3.09E-03	3.93E-02	3.32E-03
AE LMX	2.08E-01	3.68E-03	1.39E-01	3.68E-03	3.47E-01	3.68E-03	1.17E-02	4.00E-03
AE LXY	1.47E-02	4.30E-03	9.83E-03	4.30E-03	2.46E-02	4.30E-03	8.85E-04	4.70E-03
CK MMX	8.36E-01	1.21E-04	5.60E-01	1.21E-04	1.41E+00	1.21E-04	4.46E-02	1.24E-04
AE MNN	7.21E-02	5.41E-04	4.82E-02	5.41E-04	1.21E-01	5.42E-04	5.70E-03	6.17E-04
AE MNX	2.71E-04	6.88E-04	1.82E-04	6.88E-04	4.57E-04	6.90E-04	3.83E-05	7.67E-04
AE MXY	1.87E+00	4.49E-04	1.25E+00	4.50E-04	3.12E+00	4.50E-04	9.97E-02	5.05E-04
CK NNX	2.43E+00	2.49E-05	1.62E+00	2.49E-05	4.08E+00	2.49E-05	3.63E-01	3.62E-05
AE NXY	7.27E+00	2.29E-05	4.86E+00	2.29E-05	1.22E+01	2.29E-05	1.19E-01	2.62E-05
Total	13.7	-	9.2	-	23.0	-	0.70	-

In Paper II, ^{211}At was studied only considering the two main α particle emissions from ^{211}At (yield 42% and kinetic energy 5.867 MeV) and ^{211}Po (yield 58% and kinetic energy 7.450 MeV) in the dosimetric calculations.

In Paper III, the radioiodine isotopes ^{123}I, ^{125}I and ^{131}I were studied. For ^{123}I the same assumptions was made as in Paper I, but for ^{131}I the contribution from ^{131m}Xe was not considered, AE with initial kinetic energies <1 keV were assumed to deposited all their kinetic energy within the source compartment.

3.3 Monte Carlo Simulations

The MC code used for the radiation transport simulations was MCNPX 2.6.0 [75]. All MC simulations were performed on an Apple MacBook Pro with a 2.66 GHz Intel Core 2 Duo processor with Mac OS X version 10.6.8 (Apple Inc., Cupertino, California, USA). The number of simulated decays for each radiohalogen was 10^6 (Paper I), 10^7 (Paper II) and $1\text{-}5 \cdot 10^7$ (Paper III). The cut-off energy used for all simulated charged particles was 1 keV, which is the default value in MCNPX 2.6.0. The number of energy sub steps used in the simulations was 3, which is the default value for liquid water. The F6 tally in units of MeV/g (Paper II) or *F8 tally in units of MeV (Papers I and III) was used for energy deposited within the target volume. Tally F8 in units of MeV (Papers I and III) was used for the energy distribution in the target volume. Only the NR transitions were simulated, annihilation photons from the ^{124}I decay and generation of bremsstrahlung were not considered. The simulated decays were distributed homogeneously within the respective source volume or surface, and the charged particles were emitted isotropically. The radiohalogens and their daughter atoms were assumed to decay within the same source volume or surface. Recoil energy from the daughter nuclei was not considered.

3.4 Dosimetric Parameters And Calculations

The following microdosimetric parameters were calculated.

The specific energy, z, per decay is expressed as

$$z = 1.602 \cdot 10^{-13} \cdot \frac{^{*}\mathrm{F8}}{m}\ , [Gy],$$

where tally *F8 in MCNPX returns the energy deposition for the specified target volume in units of MeV. m is the mass of the target volume in units of kg, and $1.602 \cdot 10^{-13}$ is the conversion factor in units of J/MeV (Papers I and III).

$$z = 1.602 \cdot 10^{-10} \cdot \mathrm{F6}\ , [Gy],$$

where tally F6 in MCNPX returns the energy deposition averaged over the target volume in units of MeV/g, and $1.602 \cdot 10^{-10}$ is the conversion factor in units of Gy·g/MeV (Paper II).

The mean specific energy, $\langle z \rangle$, per decay *including* the discrete value of zero specific energy $(z_j = 0)$

$$\langle z \rangle = \frac{1}{N} \sum_{i=1}^{N} z_i\ , (z_i \geq 0), [Gy],$$

where N is the total number of histories simulated and z_i is the specific energy for history i (Papers I-III).

The single-hit mean specific energy, $\langle z_1 \rangle$, per decay *excluding* the discrete value of zero specific energy ($z_i > 0$).

$$\langle z_1 \rangle = \frac{1}{n} \sum_{i=1}^{n} z_i \quad (z_i > 0) \quad [Gy],$$

where n is the number of histories where $z > 0$, and z_i is the specific energy for history i (Papers I-III). When the source and target volume are the same, the mean specific energy is equal to the single-hit mean specific energy ($\langle z \rangle = \langle z_1 \rangle$).

The S value in the MIRD formalism is equivalent to $\langle z \rangle$ per decay, and was calculated for spheres (Paper I), and different source regions in the single and multiple follicle models (Papers II and III).

The mean absorbed dose, $\overline{D}$, in the target volume is calculated as

$$\overline{D} = \sum_{j=1}^{N} \tilde{A}_j \cdot \langle z \rangle_j \ , [Gy],$$

where $\tilde{A}_j$ is the time-integrated activity in the source volume, j, and $\langle z \rangle_j$ is the mean specific energy deposited in the target volume from the respective source volume j per decay (Papers II and III). $\tilde{A}_j$ can be calculated for a source volume, j, from the time-integrated specific activity, $\tilde{C}$, also called cumulative specific activity in units of Bq·s/kg.

$$\tilde{A}_j = \tilde{C} \cdot M_j \ , [Bq \cdot s],$$

where, M_j, is the mass of the source volume.

The specific energy distribution gives the distribution of the specific energy in the target volume *excluding* the discrete value of zero specific energy ($z = 0$) (Papers I-III).

The frequency-mean lineal energy, $\langle y_F \rangle$, per decay to the target volume *excluding* the discrete value $y_i = 0$ is expressed as

$$\langle y_F \rangle = \frac{1}{n} \sum_{i=1}^{n} y_i \ , (y_i > 0) \ , \ [keV/\mu m].$$

The lineal energy distribution, $f(y)$, gives the distribution of the lineal energy in the target volume *excluding* the discrete value of $y_i = 0$ (Paper II).

The mean absorbed dose, $\overline{D}_{MIRD}$, was calculated according to MIRD formalism assuming homogenous distribution of the radiohalogens within the thyroid, using nuclear decay

data from MIRD [90], calculated absorbed fractions, ϕ, (Table 3.3, Figure 4.2) and the time-integrated specific activity, $\tilde{C}_{MIRD}$ (Table 3.4).

$\tilde{C}_{MIRD}$ was derived assuming $\overline{D}_{MIRD} = 1$ Gy for ^{123}I, ^{125}I, ^{131}I and ^{211}At homogeneously distributed within the thyroid of *man*, $\phi = 1$, using nuclear decay data from MIRD [90]. $\tilde{C}_{MIRD}$ calculated for *man* was used for the species of rat and mouse (Table 3.4).

TABLE 3.3. The diameter of one thyroid lobe in the mouse, rat and human models, assuming spherical geometry, only containing follicles (no interstitial tissue), and the calculated absorbed fraction, ϕ, from the NR transitions with ^{123}I, ^{125}I, ^{131}I and ^{211}At homogeneously distributed within a thyroid follicle lobe for mouse, rat and man.

		Absorbed fraction, ϕ			
Model	Thyroid lobe diameter (mm)	^{123}I	^{125}I	^{131}I	^{211}At
Mouse	1.4	0.88	1.0	0.58	0.94
Rat	3	0.95	1.0	0.80	0.96
Man	25	1.0	1.0	1.0	1.0

For example, to achieve $\overline{D}_{MIRD} = 1$ Gy in the species of *man* with ^{211}At homogenously distributed within the thyroid, $\phi = 1$ (Table 3.3), and the mean energy per nuclear transformation from the alpha particles, $E = 6.8$ MeV resulted in $\tilde{C}_{MIRD} = 9.2 \cdot 10^{11}$ Bq·s/kg. A similar approach was used to calculate $\tilde{C}_{MIRD}$ for ^{123}I, ^{125}I and ^{131}I homogenously distributed within the thyroid of *man* (Table 3.4).

TABLE 3.4. The time integrated specific activity, $\tilde{C}_{MIRD}$, required to achieve the mean absorbed dose, $\overline{D}_{MIRD}$, of 1 Gy in the thyroid of man for ^{123}I, ^{125}I, ^{131}I and ^{211}At homogeneously distributed using MIRD formalism, assuming an absorbed fraction of 1, and nuclear decay data [90]. The time integrated specific activity, $\tilde{C}_{Lumen}$, used in the species-specific multiple thyroid follicle models of mouse, rat and man (Papers II and III) with ^{123}I, ^{125}I, ^{131}I and ^{211}At homogeneously distributed within the thyroid follicle lumens, and absent in the follicle cells, to calculate the mean absorbed dose, $\overline{D}_{PW}$, in present work (PW) to the thyroid follicle cell nuclei in the central follicle.

	^{123}I		^{125}I		^{131}I		^{211}At	
Model	$\tilde{C}_{MIRD}$ (Bq·s/kg)	$\tilde{C}_{Lumen}$ (Bq·s/kg)	$\tilde{C}_{MIRD}$ (Bq·s/kg)	$\tilde{C}_{Lumen}$ (Bq·s/kg)	$\tilde{C}_{MIRD}$ (Bq·s/kg)	$\tilde{C}_{Lumen}$ (Bq·s/kg)	$\tilde{C}_{MIRD}$ (Bq·s/kg)	$\tilde{C}_{Lumen}$ (Bq·s/kg)
Mouse	234E+12	291E+12	378E+12	488E+12	32.6E+12	40.5E+12	9.2E+11	11.8E+11
Rat	234E+12	288E+12	378E+12	483E+12	32.6E+12	40.1E+12	9.2E+11	11.7E+11
Man	234E+12	267E+12	378E+12	440E+12	32.6E+12	37.0E+12	9.2E+11	10.7E+11

$\tilde{C}_{Lumen}$ was derived from dividing $\tilde{C}_{MIRD}$ with the fraction of the total mass for the respective species-specific multiple thyroid follicle model, which is occupied with follicle

lumen (Table 3.5). Conversely, $\tilde{C}_{Cells}$ was derived by dividing $\tilde{C}_{MIRD}$ with the fraction of the total mass, which is occupied with follicle cells (Table 3.5).

TABLE 3.5. The fraction of the total mass (volume) consisting of follicle lumen (Lumen) and follicle cells (Cells) in the multiple thyroid follicle models for mouse, rat and man. These fractions are used to convert the time integrated specific activity, $\tilde{C}_{MIRD}$, used in the MIRD formalism for a homogenous distribution of the radiohalogens within the thyroid gland to, $\tilde{C}_{Lumen}$, which represent a homogenous distribution of the radiohalogens within the follicle lumens

	^{123}I		^{125}I		^{131}I		^{211}At	
Model	Lumen	Cells	Lumen	Cells	Lumen	Cells	Lumen	Cells
Mouse	0.804	0.196	0.775	0.225	0.806	0.194	0.775	0.225
Rat	0.811	0.189	0.783	0.217	0.814	0.186	0.783	0.217
Man	0.875	0.125	0.861	0.139	0.882	0.118	0.861	0.139

For example, the fraction of the total mass in the multiple thyroid follicle model of *man* for ^{211}At occupied by follicle lumen is 0.861 (Table 3.5), which results in $\tilde{C}_{Lumen} = 10.7 \cdot 10^{11}$ Bq·s/kg (Table 3.4). Conversely, if all decays would occur within the follicle cells $\tilde{C}_{MIRD} = 9.2 \cdot 10^{11}$ is divided with 0.139 (Table 3.5), resulting in $\tilde{C}_{Cells} = 66 \cdot 10^{11}$ Bq·s/kg (Table 3.4). In both cases the number of total decays occurring within the multiple thyroid follicle model are equal. Furthermore, different concentrations of the radiohalogens could be used for dosimetric calculations within the different source compartments, e.g. 90% of all the decays occurring within the follicle lumens and 10% within the follicle cells.

The mean absorbed dose, $\overline{D}_{PW}$, in present work (PW) was calculated for different species, radiohalogens, distributions, and concentrations using the multiple thyroid follicle models. $\overline{D}_{MIRD}$ was compared with $\overline{D}_{PW}$ for different species, distributions and concentrations of the radiohalogens (Table 4.1).

For example, for ^{211}At homogenously distributed within the thyroid gland of a *man* $\tilde{C}_{MIRD} = 9.2 \cdot 10^{11}$ Bq·s/kg, $\phi = 1.0$ and $E = 6.8$ MeV. Assuming a homogenous distribution within the thyroid gland according to the MIRD formalism, and using the conversion factor $1.602 \cdot 10^{-19}$ in units of J/eV, resulted in $\overline{D}_{MIRD} = 1.0$ Gy (Table 4.1).

Using the multiple thyroid model of *man* to calculate $\overline{D}_{PW}$ for ^{211}At homogenously distributed within the follicle lumens. $\tilde{C}_{Lumen} = 10.7 \cdot 10^{11}$ Bq·s/kg is multiplied with the respective mass, M_j, in units of kg, and $\langle z \rangle_j$ per decay for each source compartment (Paper II, Table 3). Each contribution from the different source compartments are then summarised, which results in $\overline{D}_{PW} = 0.71$ Gy (Table 4.1a).

4. RESULTS

4.1 PAPER I

Figure 4.1 shows ⟨z⟩ per decay from the NR transitions (equivalent to the S value) for ^{123}I, ^{124}I, ^{125}I, ^{131}I and ^{211}At as a function of the diameter for the unit density water spheres. ^{211}At had the highest ⟨z⟩ per decay for all investigated sphere sizes. The results determined with the MCNPX 2.6.0 and nuclear decay data from ICRP 107, showed in general good agreement (<10% deviation) with previously published S values, calculated using analytical and MC methods, but higher deviations were found for ^{131}I (Figure 2, Paper I).

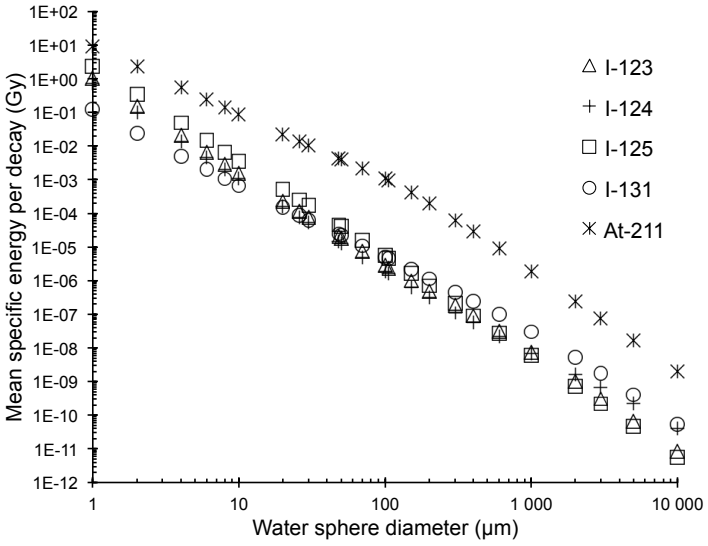

FIGURE 4.1. ⟨z⟩ per decay from the NR transitions for ^{123}I (triangle), ^{124}I (cross), ^{125}I (square), ^{131}I (circle) and ^{211}At (star) when homogeneously distributed within unit density water spheres with diameters from 1 μm to 1 cm, representing subcellular, cellular and macroscopic compartments. Note the logarithmic scale on the ordinate and abscissa (Figure 2, Paper I).

Figure 4.2 shows the absorbed fractions from the NR transitions per decay for the ^{123}I, ^{124}I, ^{125}I, ^{131}I and ^{211}At as a function of the diameter for unit density water spheres.

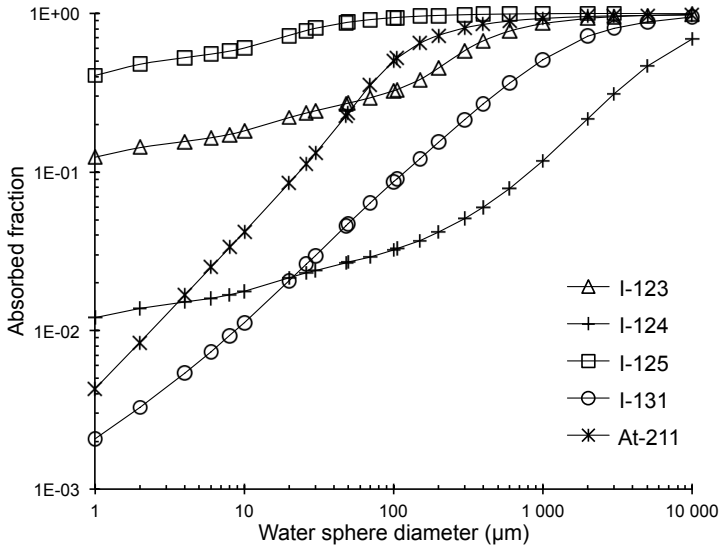

FIGURE 4.2. Absorbed fraction, ϕ, from the NR transitions for ^{123}I (triangle), ^{124}I (cross), ^{125}I (square), ^{131}I (circle) and ^{211}At (star) when homogeneously distributed within unit density water spheres with diameters from 1 μm to 1 cm. Note the logarithmic scale on the ordinate and abscissa (Figure 7, Paper I).

Figures 4.3 shows the difference in ⟨z⟩ per decay between using the average β particle energy or the full β particle energy spectrum for ^{124}I and ^{131}I homogeneously distributed in a water sphere, as a function of the water sphere diameter. For ^{124}I, the use of the average β^+ particle energy resulted in an underestimation for smaller spheres, with about 10% for 1 mm. For larger spheres there was an overestimation, which reached a maximum of 14% for the 5 mm sphere (Figure 4.3a). For ^{131}I, the use of the average β^- particle energy resulted in an underestimation in spheres up to about 270 μm with about 35%. For larger spheres there was an overestimation with a maximum of about 40% (Figure 4.3b).

Figure 4.3c shows the comparison between the ⟨z⟩ per decay calculated using the average α particle energy for ^{211}At or using the seven possible α particle energies including contributions from AE and CE, as a function of the water sphere diameter. For the smallest sphere the use of the average α particle energy underestimated ⟨z⟩ per decay with about 5% (Figure 4.3c).

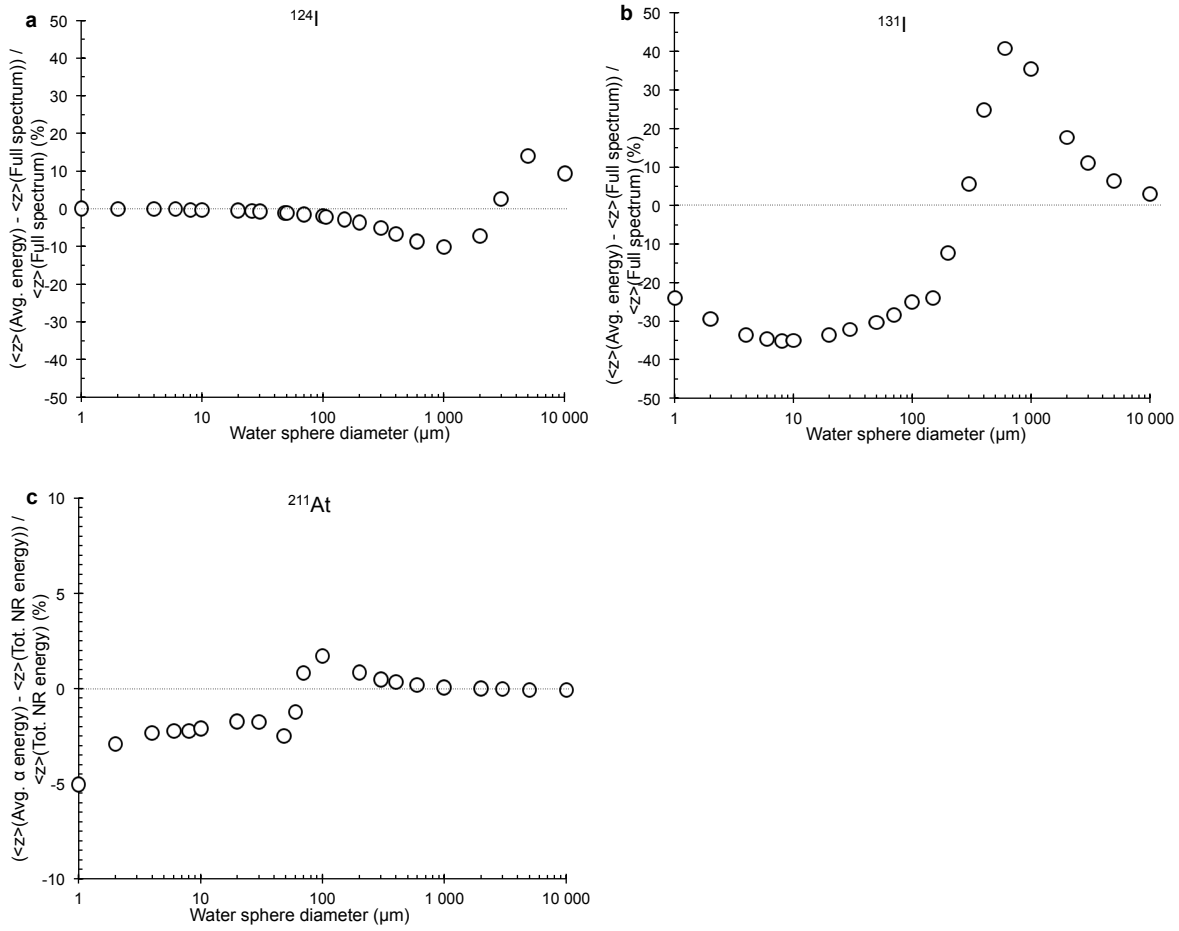

FIGURE 4.3. Comparison in per cent between ⟨z⟩ per decay calculated using the average kinetic energy (Avg. energy) and the full energy spectrum (Full spectrum) when radiohalogens were homogenously distributed within water spheres with diameters from 1 µm to 1 cm for **a)** ^{124}I using average β^+ particle energy compared with full β^+ particle energy spectrum, **b)** ^{131}I using average β^- particle energy compared with full β^- particle energy spectrum, and **c)** ^{211}At using the complete NR transitions including the seven possible α particle energies (Tot. NR energy) compared with the average α particle energy (Avg. α energy). Note the logarithmic scale on the abscissa (Figures 5b and 6, Paper I).

4.2 PAPER II

Figure 4.4 shows ⟨z⟩ per decay to the follicle cell nuclei for the mouse, rat and human models with ^{211}At homogeneously distributed within the follicle lumen, as a function of the diameter of the follicle lumen. The largest difference in ⟨z⟩ per decay between the models was for the smallest follicle diameter of 10 μm where value for the mouse model was about 35% higher than the human model. For larger follicle lumen diameters the difference in ⟨z⟩ per decay decreased, and for the 70 μm diameter follicle lumen and larger the difference remained constant at 12-13% between the mouse and human models.

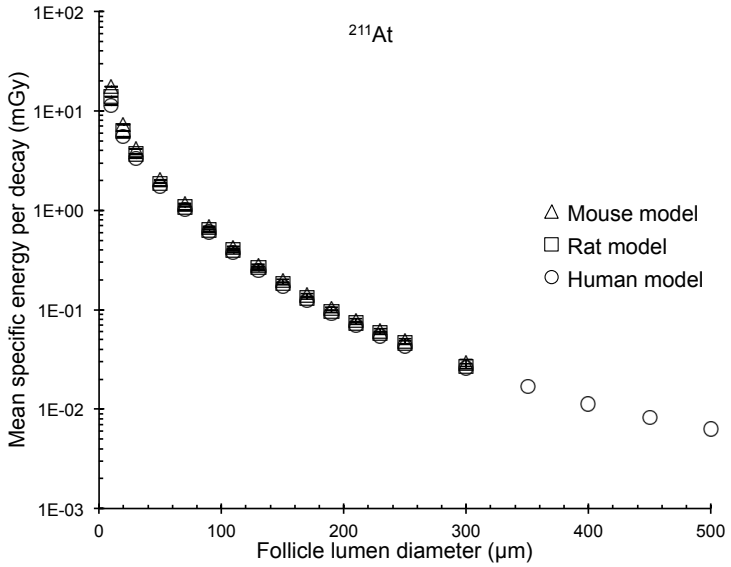

FIGURE 4.4. ⟨z⟩ per decay to the follicle cell nuclei with ^{211}At homogenously distributed within the follicle lumen for mouse (triangle), rat (square) and the human (circle), as a function of the follicle lumen diameter. The follicle lumen diameter varied from 10 μm to 300 μm for the mouse and rat, and up to 500 μm for the human model. The error bars indicate the standard deviation (SD) of the mean value, and are smaller than the data symbol when not visible. Note the logarithmic scale on the ordinate (Figure 3, Paper II).

Figure 4.5 shows ⟨z⟩ per decay to the follicle cell nuclei for the mouse, rat and human models with ^{211}At homogeneously distributed on concentric spherical shells. When decaying on the apical cell surface in the central follicles lumen the ⟨z⟩ per decay was 2.4 mGy, 1.2 mGy and 0.27 mGy for the mouse, rat and human models, respectively.

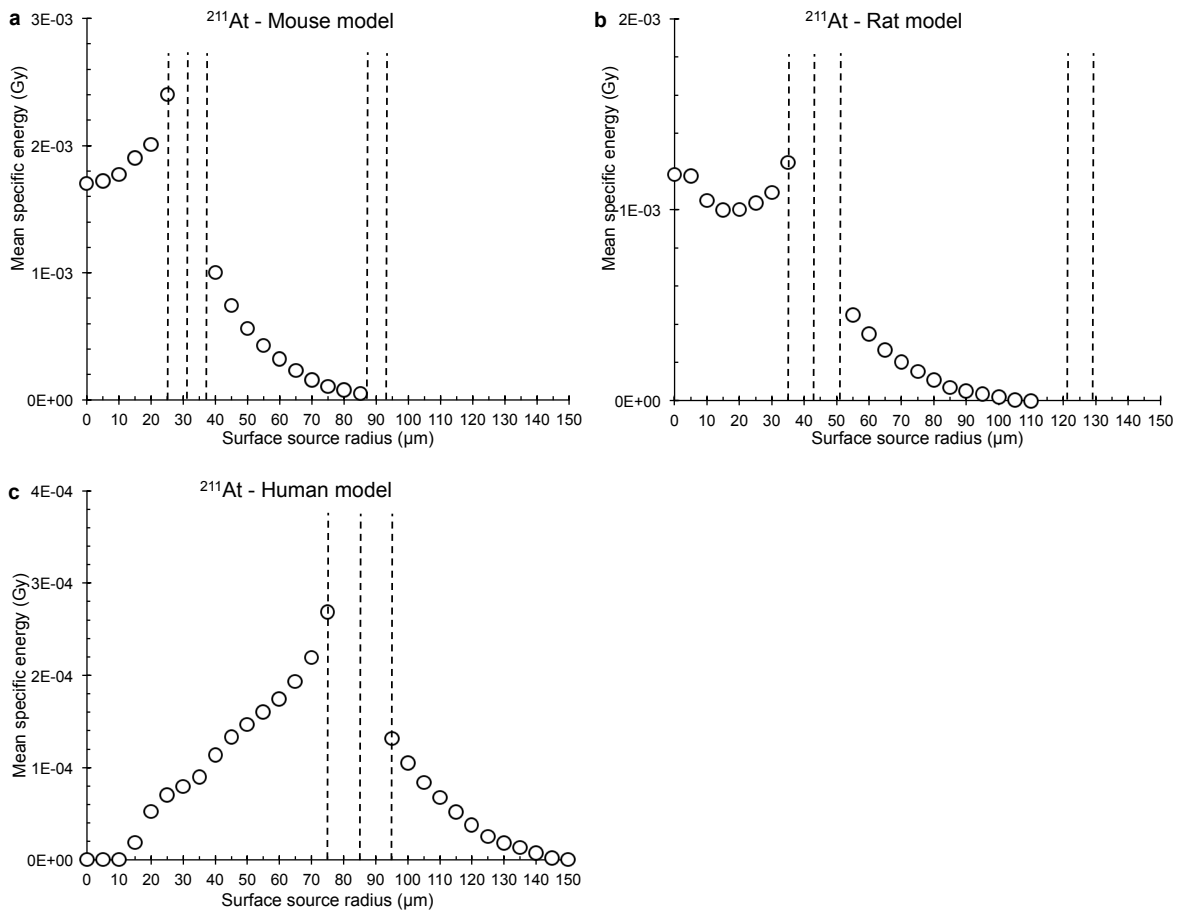

FIGURE 4.5. ⟨z⟩ per decay to the follicle cell nuclei with ^{211}At homogenously distributed on concentric spherical shells with radius from 0 μm (centrally placed point source in the follicle lumen) to 150 μm in the species-specific multiple follicle models for **a)** mouse, **b)** rat and **c)** man. The dotted lines represent the apical and basal follicle cell surfaces. The error bars indicate the standard deviation (SD) of the mean value, and are smaller than the data symbol when not visible. Data are redrawn from Figure 4, Paper II and some are previously unpublished.

Figure 4.6 shows $\langle z_1 \rangle$ per decay to the follicle cell nuclei for the mouse rat and human models with ^{211}At homogeneously distributed on concentric spherical shells. The maximum $\langle z_1 \rangle$ per decay of 2.3 Gy and 0.93 Gy for the mouse and rat models, respectively, when the decay occurred in the follicle lumens of the surrounding follicles. This occurs when the Bragg peak of the 7.45 MeV α particles coincides with the follicle cell nuclei. For the human model two maxima occurred, inside the central follicle lumen and the surrounding the follicles lumens with 0.50 Gy, respectively.

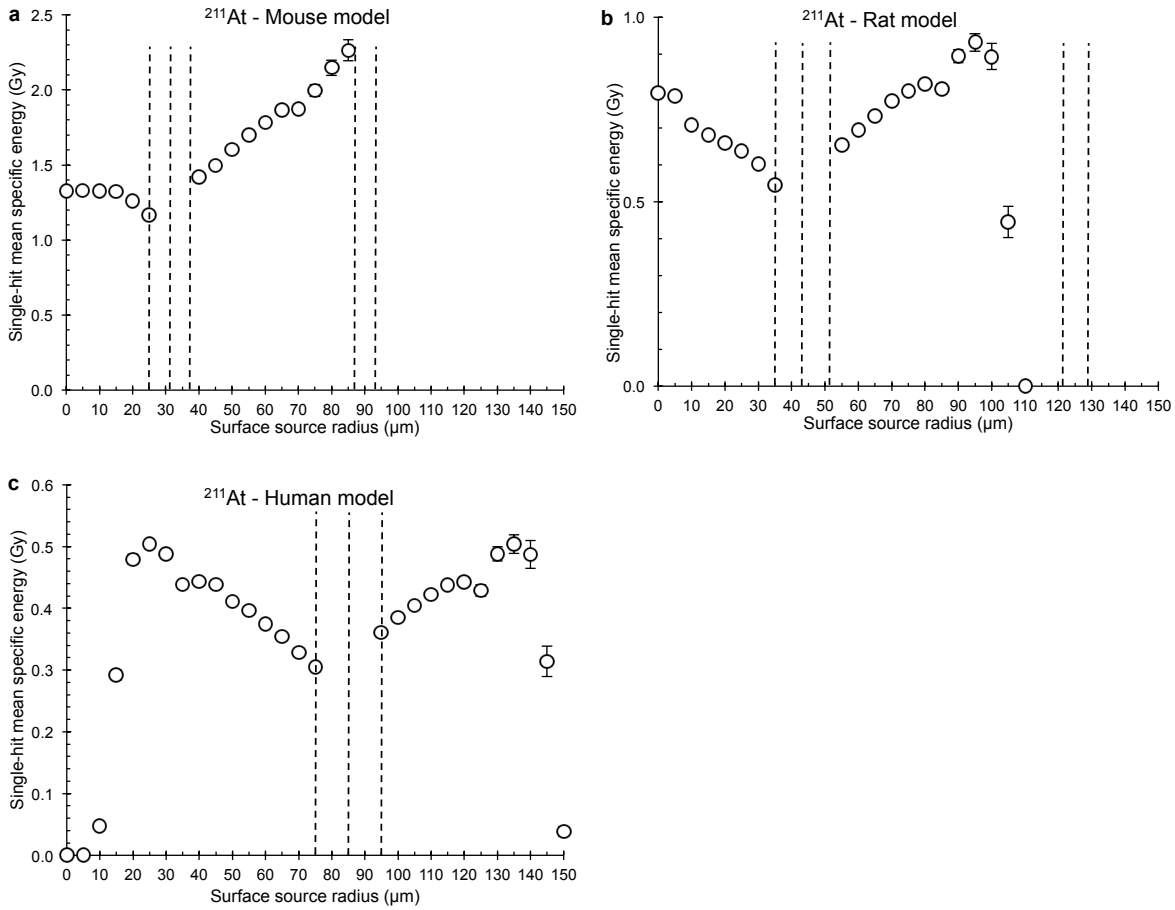

FIGURE 4.6. $\langle z_1 \rangle$ per decay to the follicle cell nuclei with ^{211}At homogenously distributed on concentric spherical shells with radius from 0 μm (centrally placed point source in the follicle lumen) to 150 μm in the species-specific multiple follicle models for **a)** mouse, **b)** rat and **c)** human. The dotted lines represent the apical and basal follicle cell surfaces. The error bars indicate the standard deviation (SD) of the mean value, and are smaller than the data symbol when not visible. Data are redrawn from Figure 6, Paper II and some are previously unpublished.

Figure 4.7 shows the specific energy distribution, $f(z)$, per decay (not showing the contribution from z = 0) in the follicle cell nuclei for the single follicle models of mouse, rat and man with ^{211}At homogenously distributed within the follicle lumen. The maximum specific energy for the mouse, rat and human model were 4.4 Gy, 1.9 Gy and 1.0 Gy, respectively. $\langle z \rangle$ per decay for the mouse, rat and human model were 2 mGy, 1.1 mGy and 0.17 mGy, respectively.

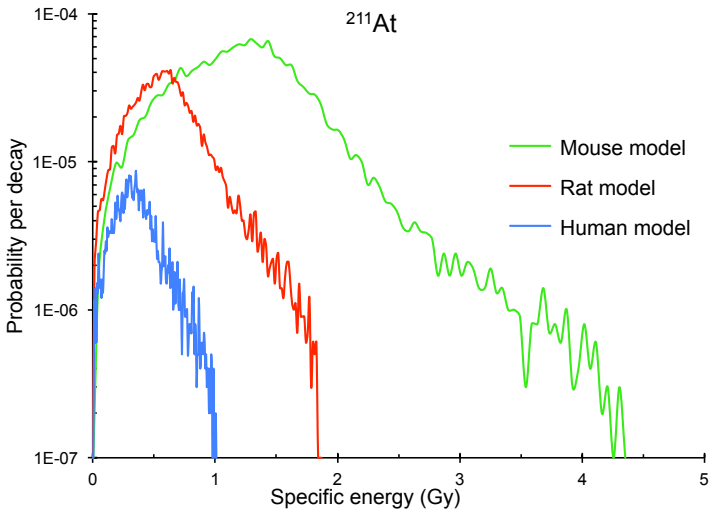

FIGURE 4.7. The specific energy distribution, *f(z),* per decay (not showing the contribution from zero specific energy, z = 0) for the mouse (green line), rat (red line) and human (blue line) single follicle models for ^{211}At homogeneously distributed within the follicle lumen. The ordinate represent the number of α particles that deposits energy within the follicle cell nuclei of the 10^7 simulated. The bin size used were 48, 14 and 6 mGy (10 keV) for the mouse, rat and human model, respectively. Note the logarithmic scale on the ordinate (Figure 7a, Paper II).

Figure 4.8 shows $\overline{D}_{PW}$ to the central follicle cell nuclei in the species-specific multiple thyroid follicle models of mouse, rat and man for different concentrations of ^{211}At, homogeneously distributed within the follicle lumens and/or follicle cells.

$\overline{D}_{PW}$ was 0.93 Gy, 0.84 Gy and 0.71 Gy with ^{211}At homogeneously distributed within the follicle lumens, and the relative contribution from the central follicle was 17%, 27% and 45% for the mouse, rat and human models, respectively (Table 4.1a).

$\overline{D}_{PW}$ was 1.3 Gy, 1.6 Gy and 2.8 Gy with ^{211}At homogeneously distributed within the follicle cells, and the relative contribution from the central follicle was 53%, 57% and 59% for the mouse, rat and human models, respectively (Table 4.1b).

$\overline{D}_{PW}$ was 1.0 Gy, 1.0 Gy and 1.0 Gy with ^{211}At homogeneously distributed within the follicle lumens and cells, and the relative contribution from the central follicle was 27%, 37% and 51% for the model of mouse, rat and man, respectively (Table 4.1c).

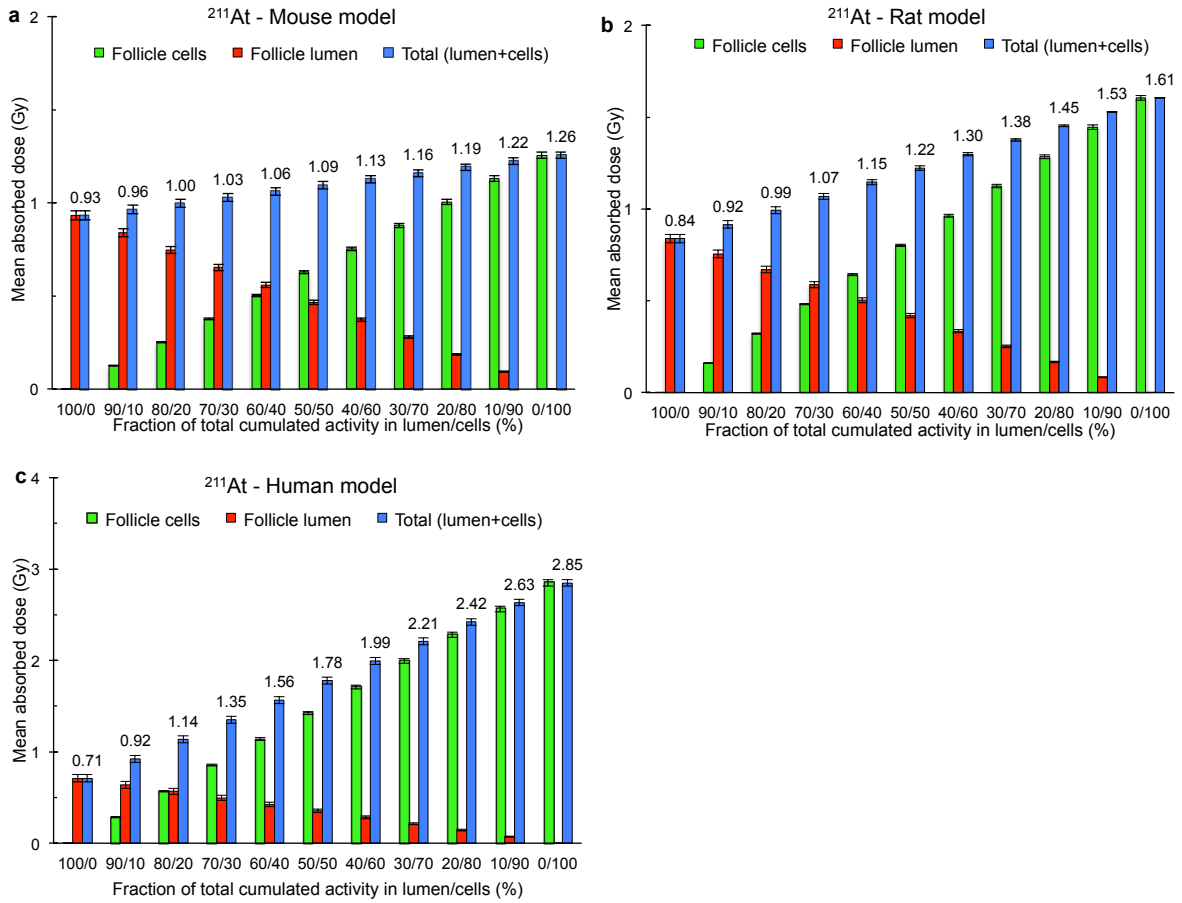

FIGURE 4.8. $\overline{D}_{PW}$ in the central follicle cell nuclei in the species-specific multiple thyroid follicle model for different relations in ^{211}At concentration (homogeneous in each compartment) between follicle lumens and/or follicle cells in the **a**) mouse model **b)** rat model and **c)** human model. The values indicate total mean absorbed dose (blue bars, numbers), and the contribution to the mean absorbed dose from the follicle lumen (red bars) and from the follicle cells (green bars). The error bars indicate the standard deviation (SD) of the mean value. The data for 100% concentration ^{211}At within the follicle lumen are taken from Paper II.

Figure 4.9 shows the fraction of the emitted α particles per decay for homogeneously distributed ^{211}At within the follicle lumen that deposit all kinetic energy within the follicle lumen, as a function of follicle lumen diameter. For the species-specific models of mouse, rat and man the fraction of the emitted α particles per decay depositing all their kinetic energy within the follicle lumen were <0.5%, 7% and 45%, respectively. For the largest follicle lumen of 500 µm about 83% of the emitted α particles per decay deposited all their kinetic energy within the follicle lumen.

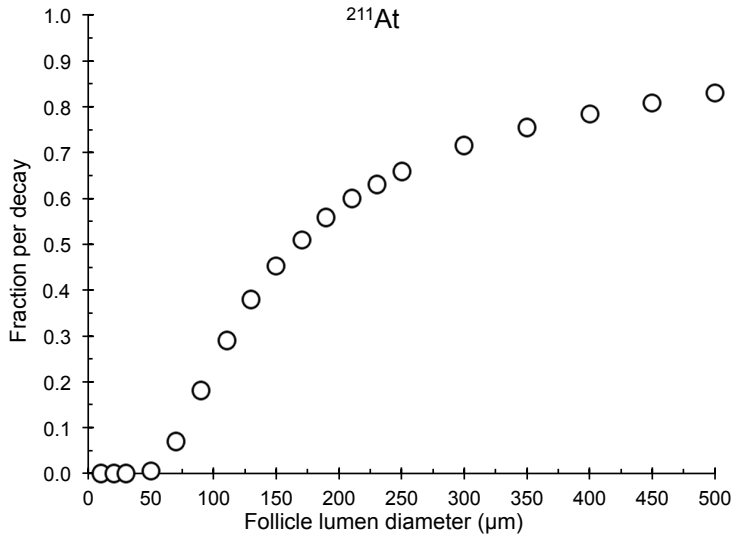

FIGURE 4.9. The fraction of the emitted α particles per decay from ^{211}At, which deposits all kinetic energy within the follicle lumen, as a function of the follicle lumen diameter. The error bars indicate the standard deviation (SD) of the mean value, and are smaller than the data symbol when not visible (Figure 8, Paper II).

4.3 PAPER III

Figures 4.10, 4.11 and 4.12 show ⟨z⟩ per decay and the relative contributions from different NR transitions for the mouse, rat and human models with ^{123}I, ^{125}I and ^{131}I homogeneously distributed within the follicle lumen, as a function of the follicle lumen diameter.

For the smallest follicle lumen diameter (10 μm) ^{125}I gave the highest ⟨z⟩ per decay, and for larger follicles ^{131}I (Figure 4.10a, 4.11a, 4.12a). The contribution from the CE was generally highest for ^{123}I and ^{125}I with exception of the small follicle lumens (Figure 4.10b-c, 4.11b-c, 4.12b-c), and the highest contribution originated from the β particles for all lumen diameters for ^{131}I (Figure 4.10d, 4.11d, 4.12d).

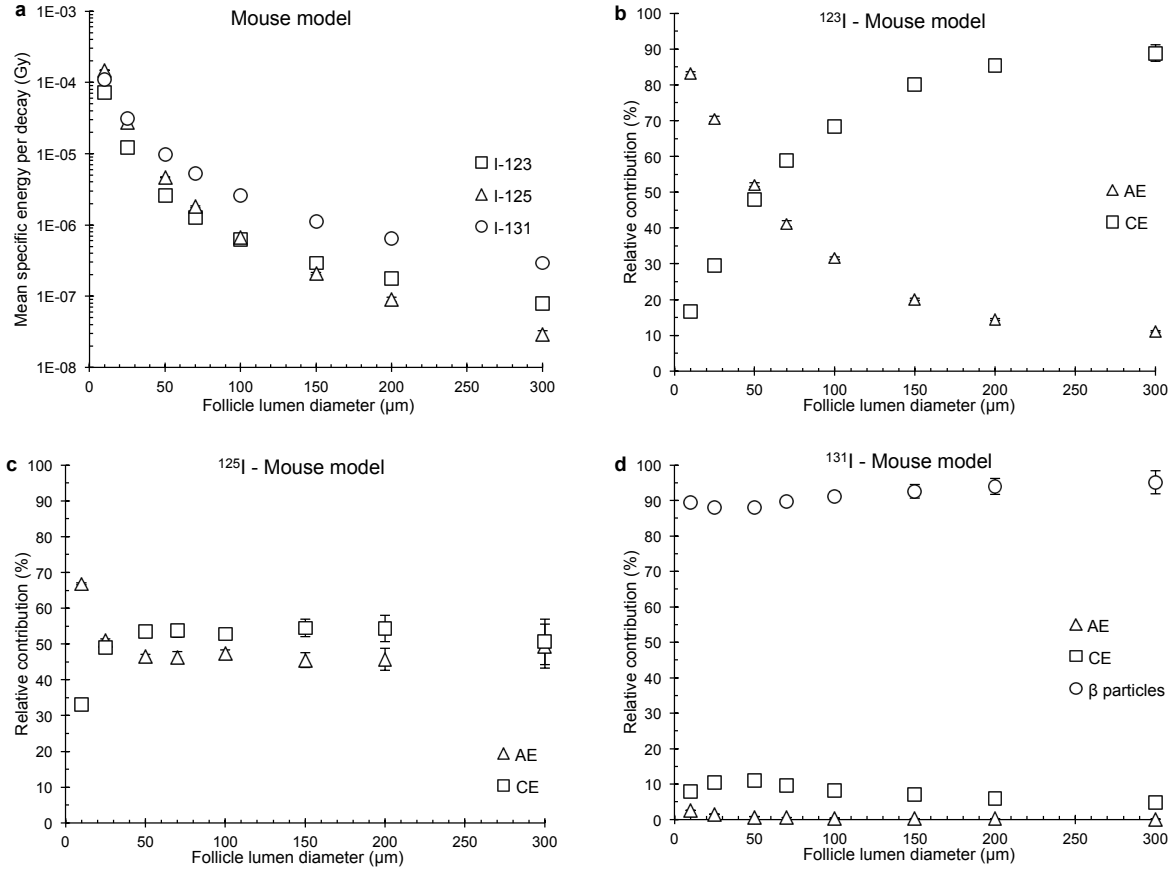

FIGURE 4.10. ⟨z⟩ per decay and the relative contribution from the NR transitions for the mouse model with radioiodine homogeneously distributed within the follicle lumen. The follicle lumen diameter varied from 10 to 300 μm surrounded with one single layer of follicle cells with a thickness of 6 μm, and centrally placed 4 μm diameter follicle cell nuclei. **a)** The total ⟨z⟩ per decay to the follicle cell nucleus for ^{123}I (square), ^{125}I (triangle) and ^{131}I (circle), as a function of the follicle lumen diameter. Note the logarithmic scale on the ordinate. **b-d)** The relative contribution per decay in per cent to the follicle cell nuclei from AE (triangle), CE (square), β particles (circle), as a function of the follicle lumen diameter, for **b)** ^{123}I, **c)** ^{125}I and **d)** ^{131}I. Error bars indicate the standard deviation of the mean value (SD) and are smaller than the symbol when not visible.

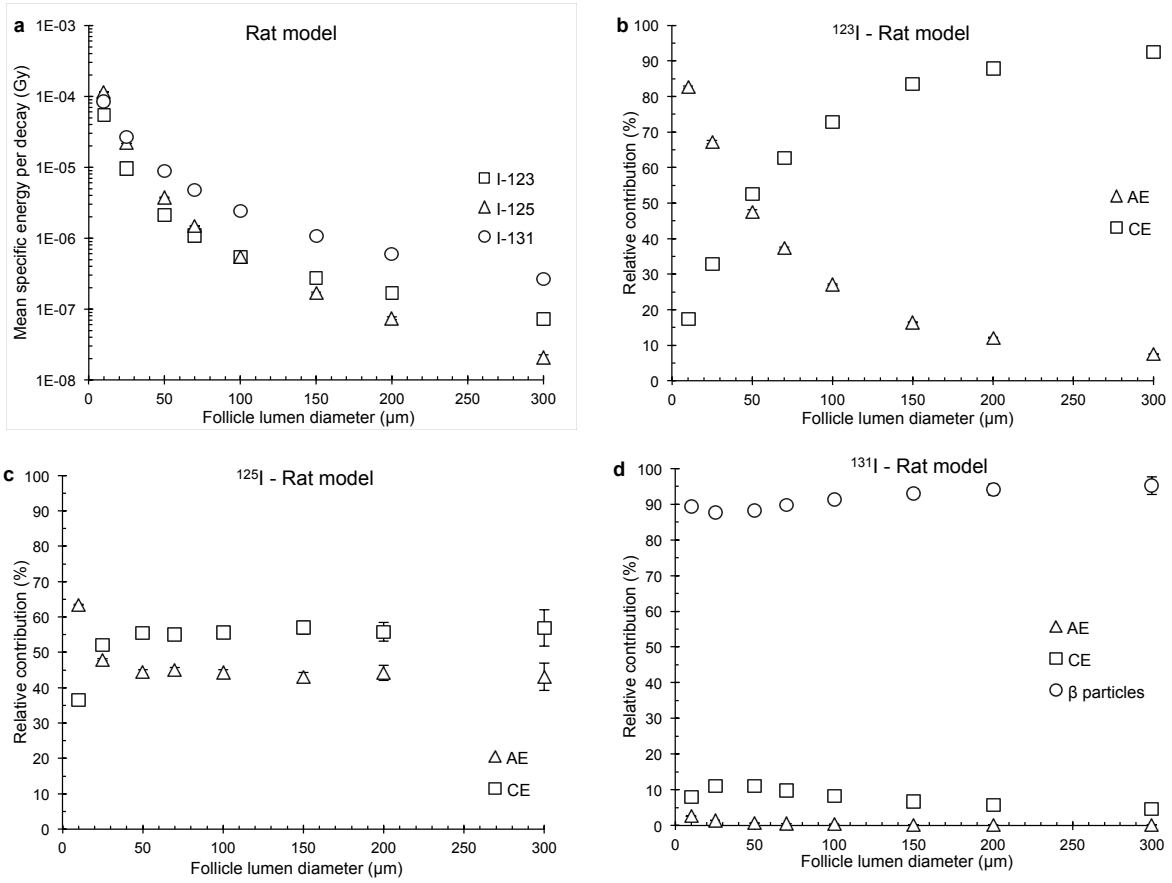

FIGURE 4.11. ⟨z⟩ per decay and the relative contribution from the NR transitions for the rat model with radioiodine homogeneously distributed within the follicle lumen. The follicle lumen diameter varied from 10 to 300 μm surrounded with one single layer of follicle cells with a thickness of 8 μm, and centrally placed 6 μm diameter follicle cell nuclei. **a)** The total ⟨z⟩ per decay to the follicle cell nucleus for ^{123}I (square), ^{125}I (triangle) and ^{131}I (circle), as a function of the follicle lumen diameter. Note the logarithmic scale on the ordinate. **b-d)** The relative contribution per decay in per cent to the follicle cell nuclei from AE (triangle), CE (square), β particles (circle), as a function of the follicle lumen diameter, for **b)** ^{123}I, **c)** ^{125}I and **d)** ^{131}I. Error bars indicate the standard deviation of the mean value (SD) and are smaller than the symbol when not visible.

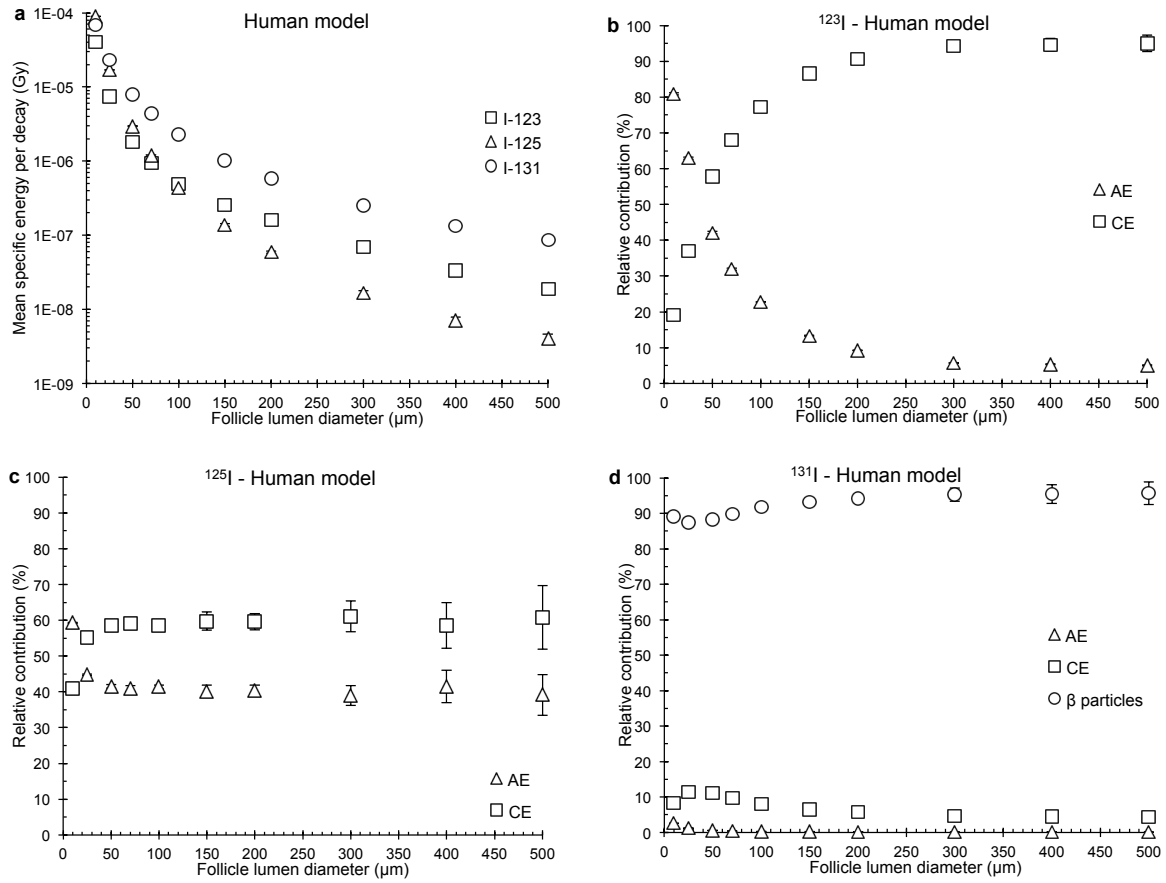

FIGURE 4.12. ⟨z⟩ per decay and the relative contribution from the NR transitions for the human model with radioiodine homogeneously distributed within the follicle lumen. The follicle lumen diameter varied from 10 to 500 μm surrounded with one single layer of follicle cells with a thickness of 10 μm, and centrally placed 8 μm diameter follicle cell nuclei. **a)** The total ⟨z⟩ per decay to the follicle cell nucleus for ^{123}I (square), ^{125}I (triangle) and ^{131}I (circle), as a function of the follicle lumen diameter. Note the logarithmic scale on the ordinate. **b-d)** The relative contribution per decay in per cent to the follicle cell nuclei from AE (triangle), CE (square), β particles (circle), as a function of the follicle lumen diameter, for **b)** ^{123}I, **c)** ^{125}I and **d)** ^{131}I. Error bars indicate the standard deviation of the mean value (SD) and are smaller than the symbol when not visible (Figure 1, Paper III).

Figure 4.13 shows ⟨z⟩ per decay to the follicle cell nuclei for the models of mouse, rat and man with ^{123}I homogeneously distributed on concentric spherical shells, as a function of this surface source radius. The contributions from the AE and CE are shown as well as the total ⟨z⟩ per decay. When decaying on the apical cell surface in the central follicles lumen the ⟨z⟩ per decay was 4.9 μGy, 2.3 μGy and 0.55 μGy for the mouse, rat and human models, respectively. The corresponding relative contribution from AE was 69%, 64% and 50% for the mouse, rat and human models, respectively.

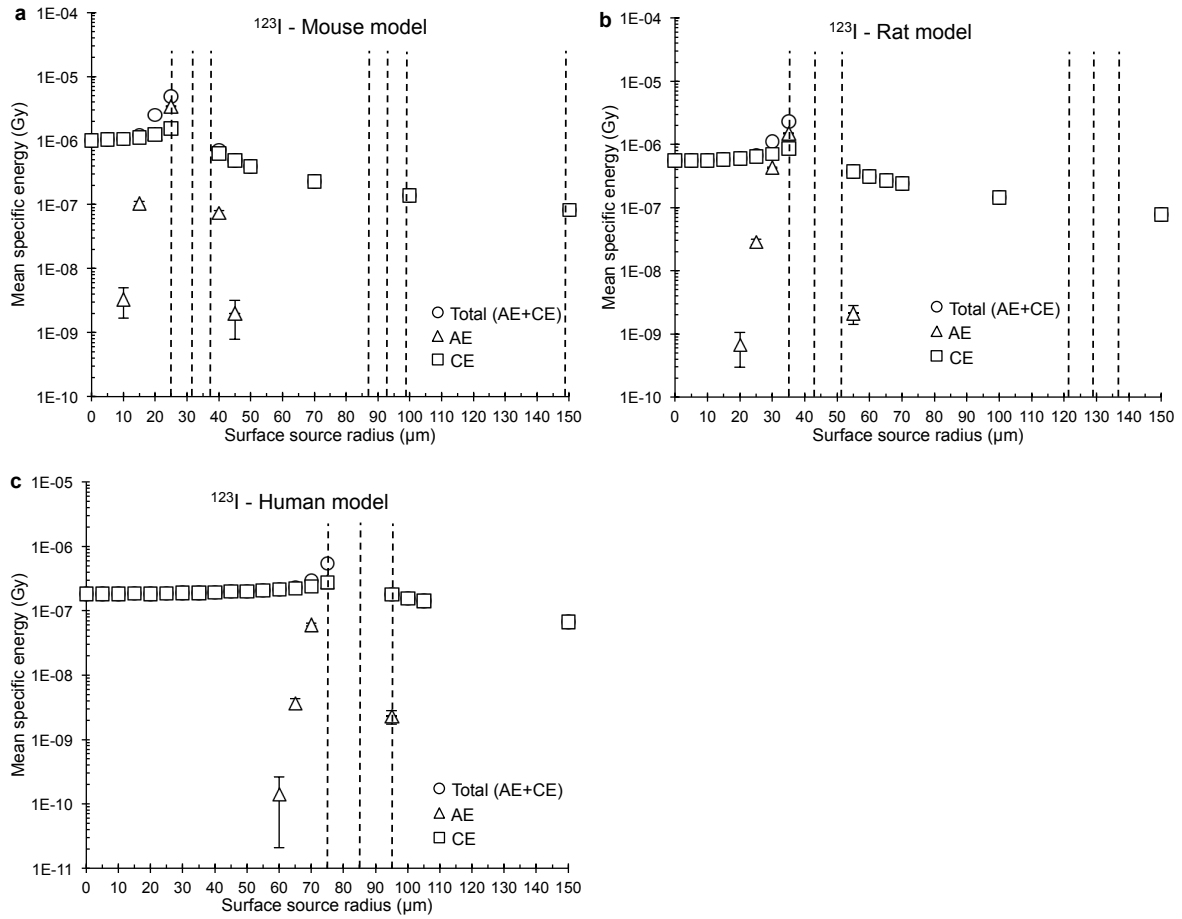

FIGURE 4.13. ⟨z⟩ per decay to the follicle cell nuclei from the NR transitions with ^{123}I homogeneously distributed on concentric spherical shells in the thyroid follicle models of **a)** mouse, **b)** rat, and **c)** man. The contribution from AE (triangle) and CE (square) are shown separately, together with the total value (circle). The surface source radius 0 µm indicates the centre of the follicle lumen, and the dotted lines represent the apical and basal follicle cell surfaces for the respective models. Error bars indicate the standard deviation of the mean value (SD) and are smaller than the symbol when not visible. Note the logarithmic scale on the ordinate (Figure 2a, Paper III).

Figure 4.14 shows ⟨z⟩ per decay to the follicle cell nuclei for the models of mouse, rat and man with ^{125}I homogeneously distributed on concentric spherical shells, as a function of this surface source radius. When decaying on the apical cell surface in the central follicles lumen ⟨z⟩ per decay was 9.3 µGy, 4.1 µGy and 0.81 µGy for the mouse, rat and human models, respectively. The corresponding relative contribution from AE was 59%, 58% and 56% for the mouse, rat and human models, respectively.

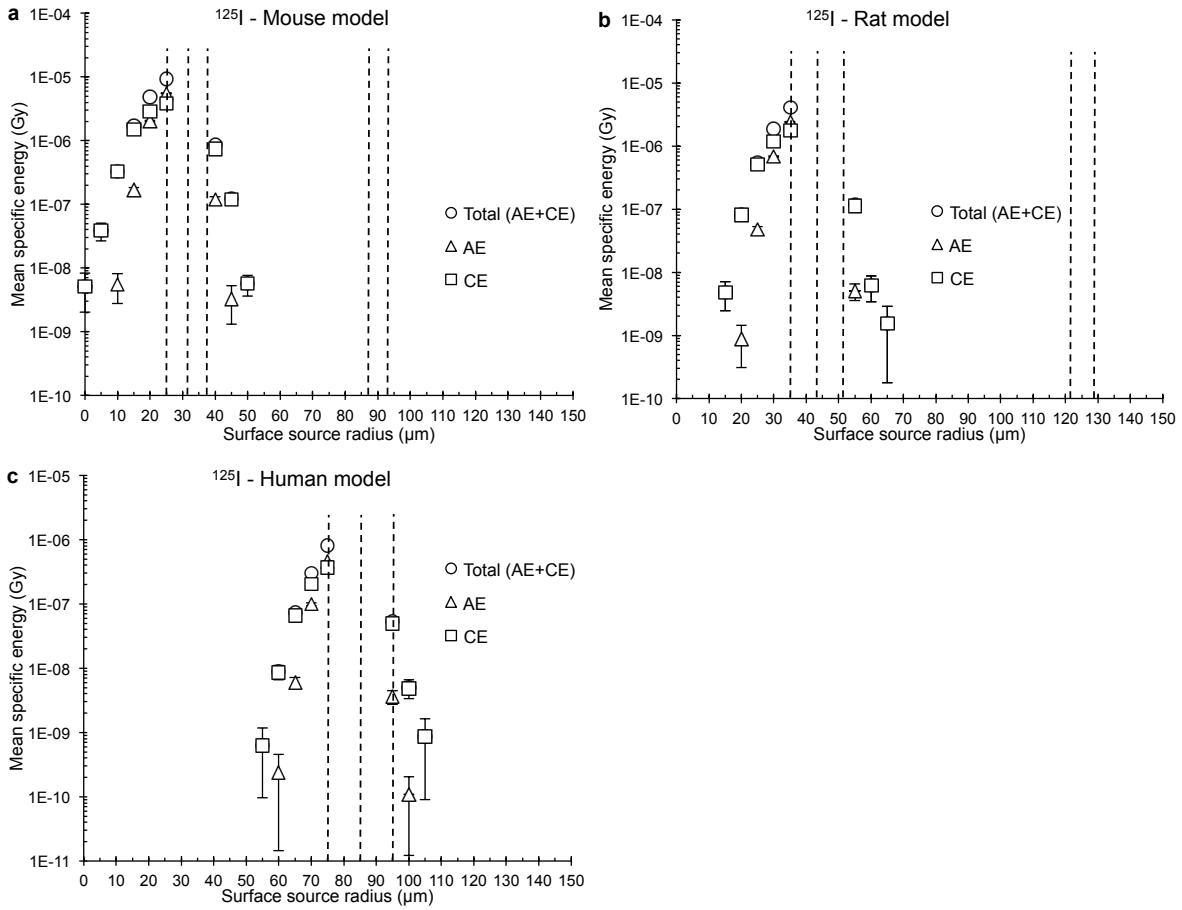

FIGURE 4.14. ⟨z⟩ per decay to the follicle cell nuclei from the NR transitions with ^{125}I homogeneously distributed on concentric spherical shells in the thyroid follicle models of **a)** mouse, **b)** rat, and **c)** man. The contribution from AE (triangle) and CE (square) are shown separately, together with the total value (circle). The surface source radius 0 μm indicates the centre of the follicle lumen, and the dotted lines represent the apical and basal follicle cell surfaces for the respective models. Error bars indicate the standard deviation of the mean value (SD) and are smaller than the symbol when not visible. Note the logarithmic scale on the ordinate (Figure 2b, Paper III).

Figure 4.15 shows ⟨z⟩ per decay to the follicle cell nuclei for the models of mouse, rat and man with ^{131}I homogeneously distributed on concentric spherical shells, as a function of this surface source radius. The contributions from the AE, CE and β^- particles are shown as well as the total ⟨z⟩ per decay. When decaying on the apical cell surface in the central follicles lumen ⟨z⟩ per decay was 12.4 μGy, 6.3 μGy and 1.6 μGy for the mouse, rat and human models, respectively. The corresponding relative contribution from β^- particles was 89%, 90% and 91% for the mouse, rat and human models, respectively.

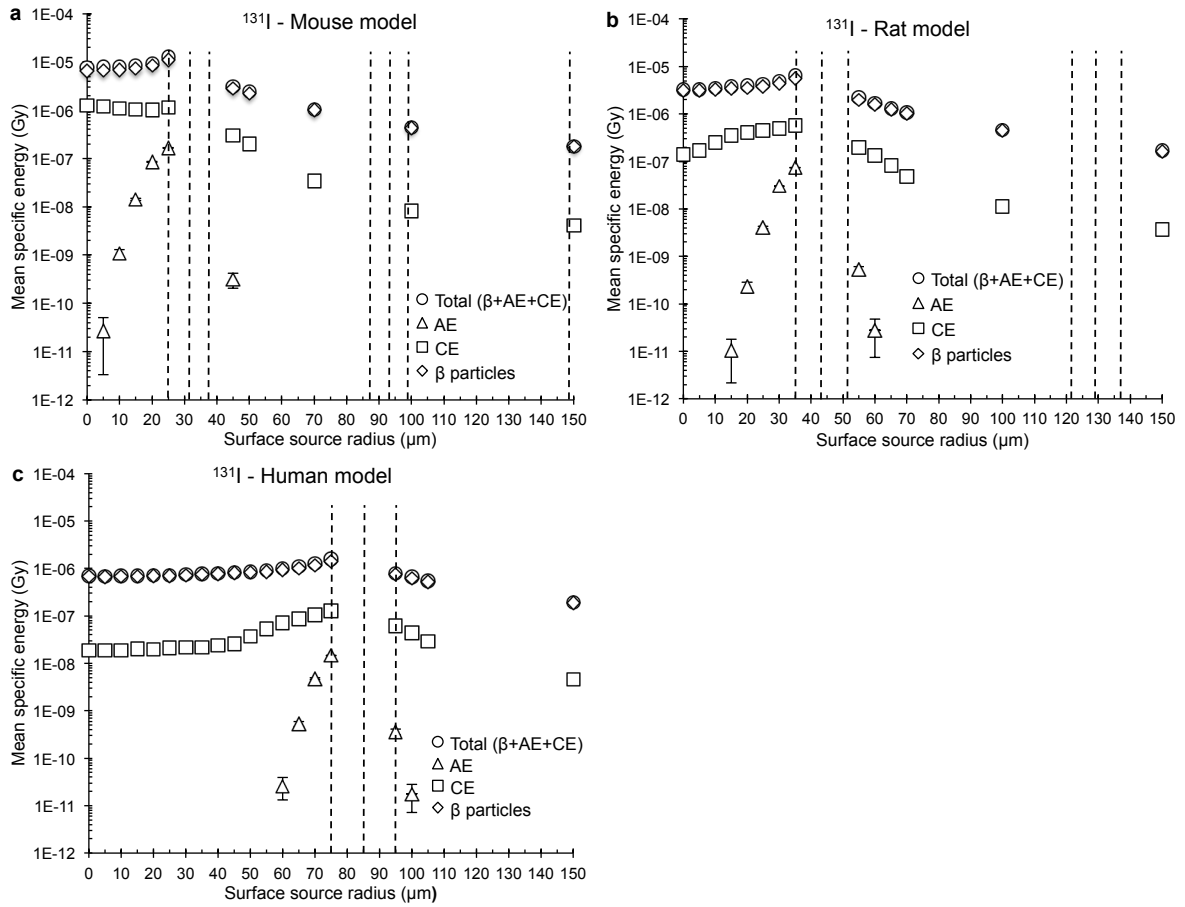

FIGURE 4.15. ⟨z⟩ per decay to the follicle cell nuclei from the NR transitions from ^{131}I homogeneously distributed on concentric spherical shells in the thyroid follicle models of **a)** mouse, **b)** rat and **c)** man. The contribution from AE (triangle), CE (square) and β^- particles (diamond) are shown separately, together with the total value (circle). The surface source radius 0 μm indicates the centre of the follicle lumen, and the dotted lines represent the apical and basal follicle cell surfaces for the respective models. Error bars indicate the standard deviation of the mean value (SD) and are smaller than the symbol when not visible. Note the logarithmic scale on the ordinate (Figure 2c, Paper III).

Figure 4.16 shows $\overline{D}_{PW}$ to the central follicle cell nuclei in the species-specific multiple thyroid follicle models of mouse, rat and man for different relations in ^{123}I concentration for homogeneous distributions between follicle lumens and/or follicle cells.

$\overline{D}_{PW}$ was 0.82 Gy, 0.81 Gy and 0.80 Gy for ^{123}I homogeneously distributed within the follicle lumens, and the relative contribution from the central follicle was 6%, 7% and 15% in the models of mouse, rat and man, respectively (Table 4.1a).

$\overline{D}_{PW}$ was 2.2 Gy, 2.3 Gy and 3.1 Gy for ^{123}I homogeneously distributed within the follicle cells, and the relative contribution from the central follicle was 57%, 62% and 77% in the models of mouse, rat and man, respectively (Table 4.1b).

$\overline{D}_{PW}$ was 1.08 Gy, 1.09 Gy and 1.09 Gy with ^{123}I homogeneously distributed within the follicle lumens and cells, and the relative contribution from the central follicle was 26%, 29% and 37% for the model of mouse, rat and man, respectively (Table 4.1c).

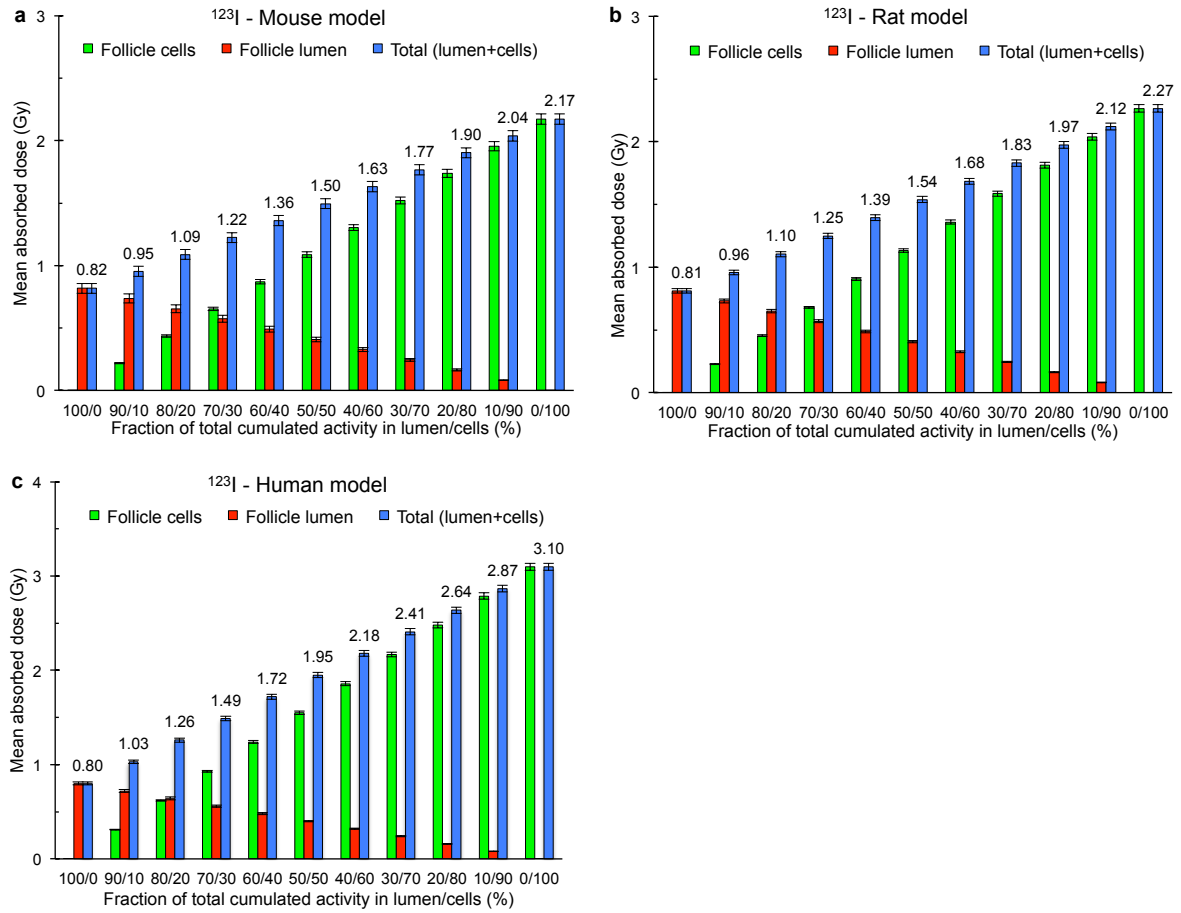

FIGURE 4.16. $\overline{D}_{PW}$ in the central follicle cell nuclei in the species-specific multiple thyroid follicle model for different relations in ^{123}I concentration (homogeneous in each compartment) between follicle lumens and/or follicle cells for **a**) mouse model **b)** rat model and **c)** human model. The values indicate total mean absorbed dose (blue bars, numbers), and the contribution to the mean absorbed dose from the follicle lumen (red bars) and from the follicle cells (green bars). The error bars indicate the standard deviation (SD) of the mean value (Figure 5a, Paper III).

Figure 4.17 shows $\overline{D}_{PW}$ to the central follicle cell nuclei in the species-specific multiple thyroid follicle models of mouse, rat and man for different relations in ^{125}I concentration for homogeneous distributions between follicle lumens and/or follicle cells.

$\overline{D}_{PW}$ was 0.21 Gy, 0.15 Gy and 0.11 Gy for ^{125}I homogeneously distributed within the follicle lumens, and the relative contribution from the central follicle was 70%, 84% and 94% for the model of mouse, rat and man, respectively (Table 4.1a).

$\overline{D}_{PW}$ was 4.5 Gy, 4.9 Gy and 7.8 Gy for ^{125}I homogeneously distributed within the follicle cells, and the relative contribution from the central follicle was 86%, 87% and 90% for the model of mouse, rat and man, respectively (Table 4.1b).

$\overline{D}_{PW}$ was 1.17 Gy, 1.17 Gy and 1.18 Gy with ^{125}I homogeneously distributed within the follicle lumens and cells, and the relative contribution from the central follicle was 84%, 87% and 90% for the model of mouse, rat and man, respectively (Table 4.1c).

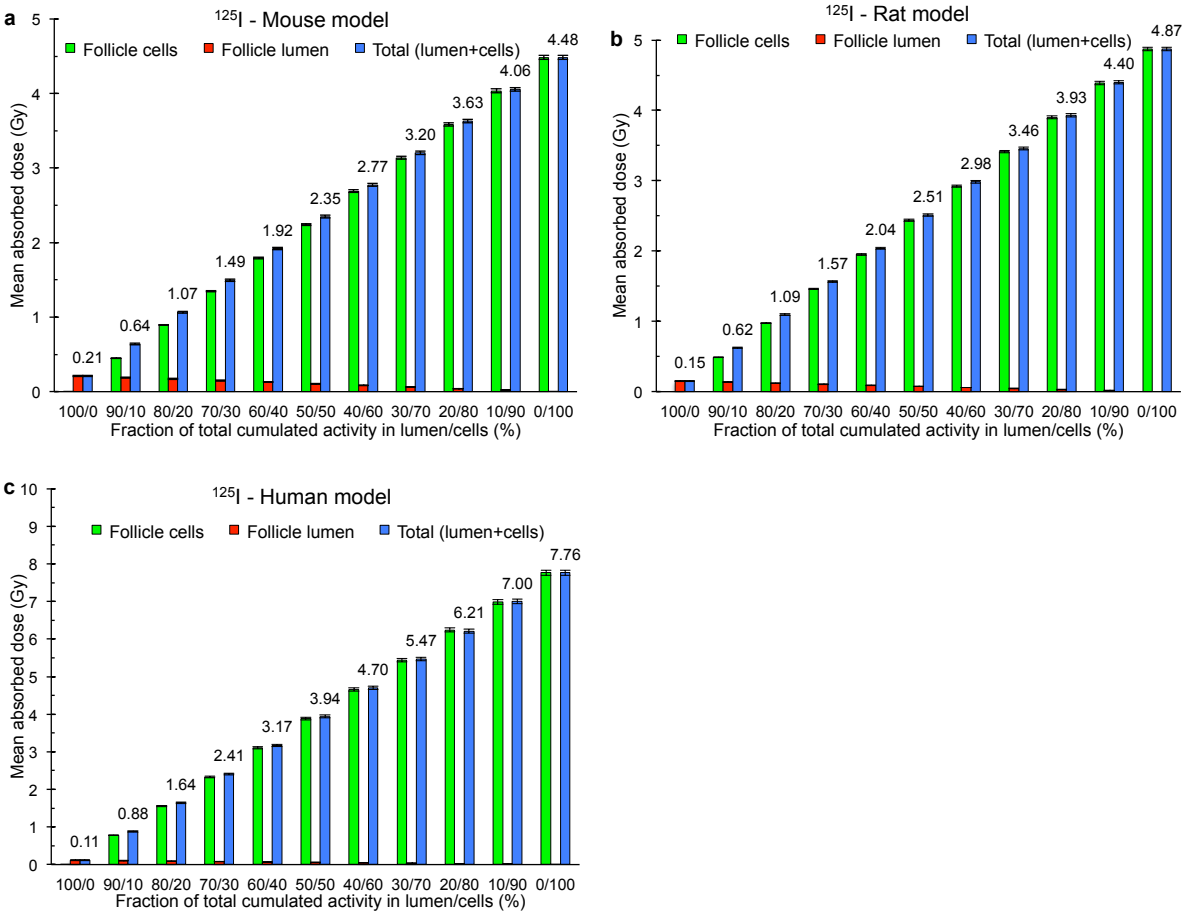

FIGURE 4.17. $\overline{D}_{PW}$ in the central follicle cell nuclei in the species-specific multiple thyroid follicle model for different relations in ^{125}I concentration (homogeneous in each compartment) between follicle lumens and/or follicle cells for **a**) mouse model **b)** rat model and **c)** human model. The values indicate total mean absorbed dose (blue bars, numbers), and the contribution to the mean absorbed dose from the follicle lumen (red bars) and from the follicle cells (green bars). The error bars indicate the standard deviation (SD) of the mean value (Figure 5b, Paper III).

Figure 4.18 shows $\overline{D}_{PW}$ to the central follicle cell nuclei in the species-specific multiple thyroid follicle models of mouse, rat and man for different relations in ^{131}I concentration for homogeneous distributions between follicle lumens and/or follicle cells.

$\overline{D}_{PW}$ was 0.78 Gy, 1.01 Gy and 0.98 Gy with ^{131}I homogeneously distributed within the follicle lumens, and the relative contribution from the central follicle was 3.3%, 3.4% and 6.9% for the model of mouse, rat and man, respectively (Table 4.1a).

$\overline{D}_{PW}$ was 0.95 Gy, 1.2 Gy and 1.5 Gy with ^{131}I homogeneously distributed within the follicle cells, and the relative contribution from the central follicle was 16%, 17% and 30% for the model of mouse, rat and man, respectively (Table 4.1b).

$\overline{D}_{PW}$ was 0.81 Gy, 1.05 Gy and 1.04 Gy with ^{131}I homogeneously distributed within the follicle lumens and cells, and the relative contribution from the central follicle was 6%, 6% and 11% for the model of mouse, rat and man, respectively (Table 4.1c).

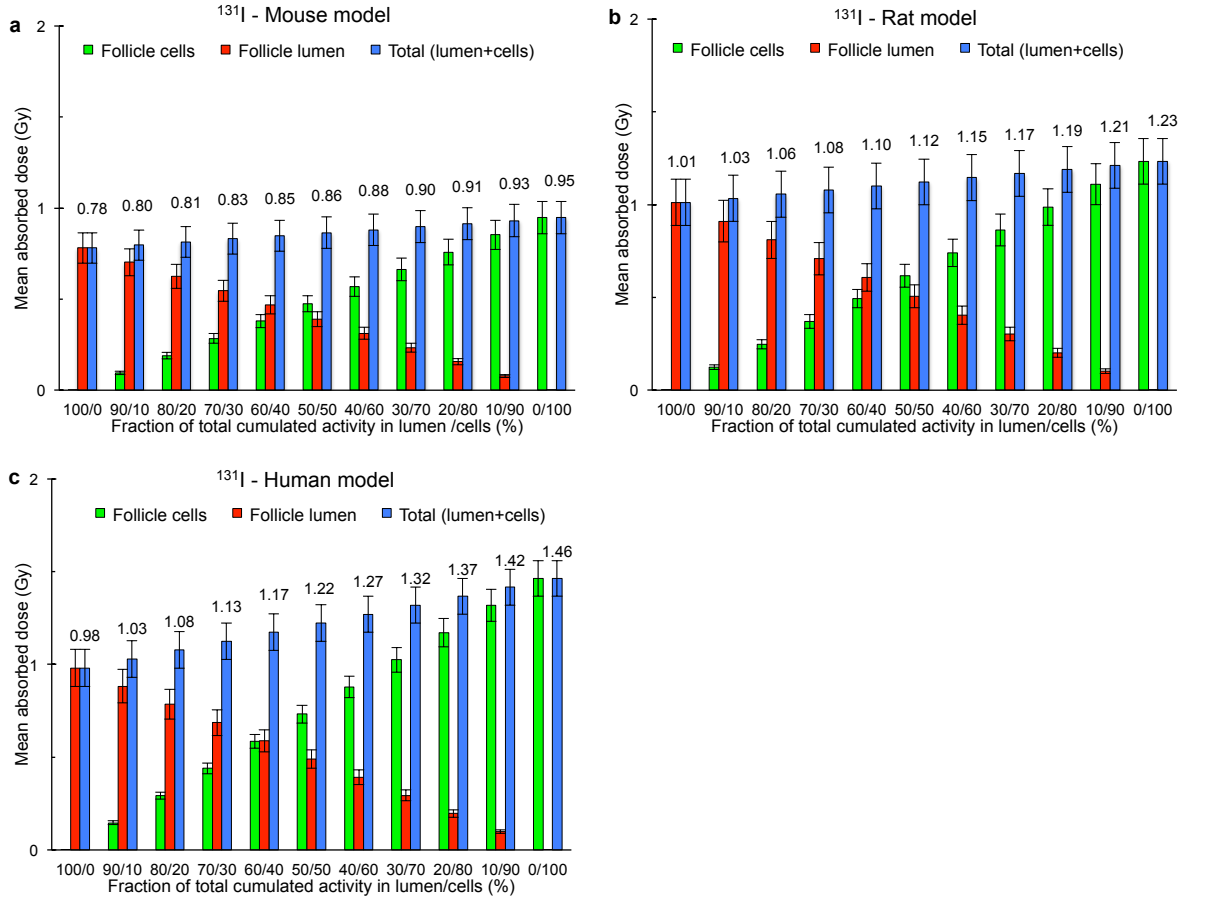

FIGURE 4.18. $\overline{D}_{PW}$ in the central follicle cell nuclei in the species-specific multiple thyroid follicle model for different relations in ^{131}I concentration (homogeneous in each compartment) between follicle lumens and/or follicle cells for **a**) mouse model **b)** rat model and **c)** human model. The values indicate total mean absorbed dose (blue bars, numbers), and the contribution to the mean absorbed dose from the follicle lumen (red bars) and from the follicle cells (green bars). The error bars indicate the standard deviation (SD) of the mean value (Figure 5c, Paper III).

TABLE 4.1. The calculated mean absorbed dose, $\overline{D}_{MIRD}$, in the thyroid with ^{123}I, ^{125}I, ^{131}I and ^{211}At homogeneously distributed, with the time integrated specific activity, $\tilde{C}_{MIRD}$, (Table 3.4), nuclear decay data from MIRD [90], and calculated absorbed fractions (Table 3.3). The time integrated specific activity, $\tilde{C}_{Lumen}$, used in the multiple thyroid follicle models of mouse, rat and man with ^{123}I, ^{125}I, ^{131}I (Paper III) and ^{211}At (Paper II) homogeneously distributed within the follicle lumens, and $\tilde{C}_{Cells}$ used when homogenously distributed within the follicle cells, to calculate $\overline{D}_{PW}$ in the thyroid follicle nuclei in the central follicle. The numbers within the brackets represent the difference in per cent for $\overline{D}_{MIRD}$ compared with $\overline{D}_{PW}$.

a) The radiohalogens homogeneously distributed within the follicle lumens.

	^{123}I		^{125}I		^{131}I		^{211}At	
	$\overline{D}_{MIRD}$	$\overline{D}_{PW}$	$\overline{D}_{MIRD}$	$\overline{D}_{PW}$	$\overline{D}_{MIRD}$	$\overline{D}_{PW}$	$\overline{D}_{MIRD}$	$\overline{D}_{PW}$
Model	(Gy)	(Gy)	(Gy)	(Gy)	(Gy)	(Gy)	(Gy)	(Gy)
Mouse	0.88 (+7.3%)	0.82	1.0 (+380%)	0.21	0.58 (-26%)	0.78	0.94 (+1.1%)	0.93
Rat	0.95 (+17%)	0.81	1.0 (+570%)	0.15	0.80 (-21%)	1.01	0.96 (+14%)	0.84
Man	1.0 (+25%)	0.80	1.0 (+810%)	0.11	1.0 (+2.0%)	0.98	1.0 (+41%)	0.71

b) The radiohalogens homogeneously distributed within the follicle cells.

	^{123}I		^{125}I		^{131}I		^{211}At	
	$\overline{D}_{MIRD}$	$\overline{D}_{PW}$	$\overline{D}_{MIRD}$	$\overline{D}_{PW}$	$\overline{D}_{MIRD}$	$\overline{D}_{PW}$	$\overline{D}_{MIRD}$	$\overline{D}_{PW}$
Model	(Gy)	(Gy)	(Gy)	(Gy)	(Gy)	(Gy)	(Gy)	(Gy)
Mouse	0.88 (-59%)	2.2	1.0 (-78%)	4.5	0.58 (-39%)	0.95	0.94 (-25%)	1.3
Rat	0.95 (-58%)	2.3	1.0 (-79%)	4.9	0.80 (-35%)	1.2	0.96 (-40%)	1.6
Man	1.0 (-68%)	3.1	1.0 (-87%)	7.8	1.0 (-32%)	1.5	1.0 (-65%)	2.8

c) The radiohalogens homogeneously distributed within the follicle lumens and cells.

	^{123}I		^{125}I		^{131}I		^{211}At	
	$\overline{D}_{MIRD}$	$\overline{D}_{PW}$	$\overline{D}_{MIRD}$	$\overline{D}_{PW}$	$\overline{D}_{MIRD}$	$\overline{D}_{PW}$	$\overline{D}_{MIRD}$	$\overline{D}_{PW}$
Model	(Gy)	(Gy)	(Gy)	(Gy)	(Gy)	(Gy)	(Gy)	(Gy)
Mouse	0.88 (-19%)	1.08	1.0 (-15%)	1.17	0.58 (-28%)	0.81	0.94 (-6.0%)	1.0
Rat	0.95 (-13%)	1.09	1.0 (-15%)	1.17	0.80 (-24%)	1.05	0.96 (-4.0%)	1.0
Man	1.0 (-8.3%)	1.09	1.0 (-15%)	1.18	1.0 (-3.8%)	1.04	1.0 (±0.0%)	1.0

Figure 4.19 shows $f(z)$ per decay (not showing the contribution from z = 0) in the follicle cell nuclei for the single follicle model of mouse, with ^{123}I, ^{125}I and ^{131}I homogenously distributed within the follicle lumen. The maximum specific energy for ^{123}I, ^{125}I and ^{131}I was 84 mGy, 89 mGy and 93 mGy, respectively. $\langle z \rangle$ per decay for ^{123}I, ^{125}I and ^{131}I was 2.6 µGy, 4.7 µGy and 9.7 µGy, respectively.

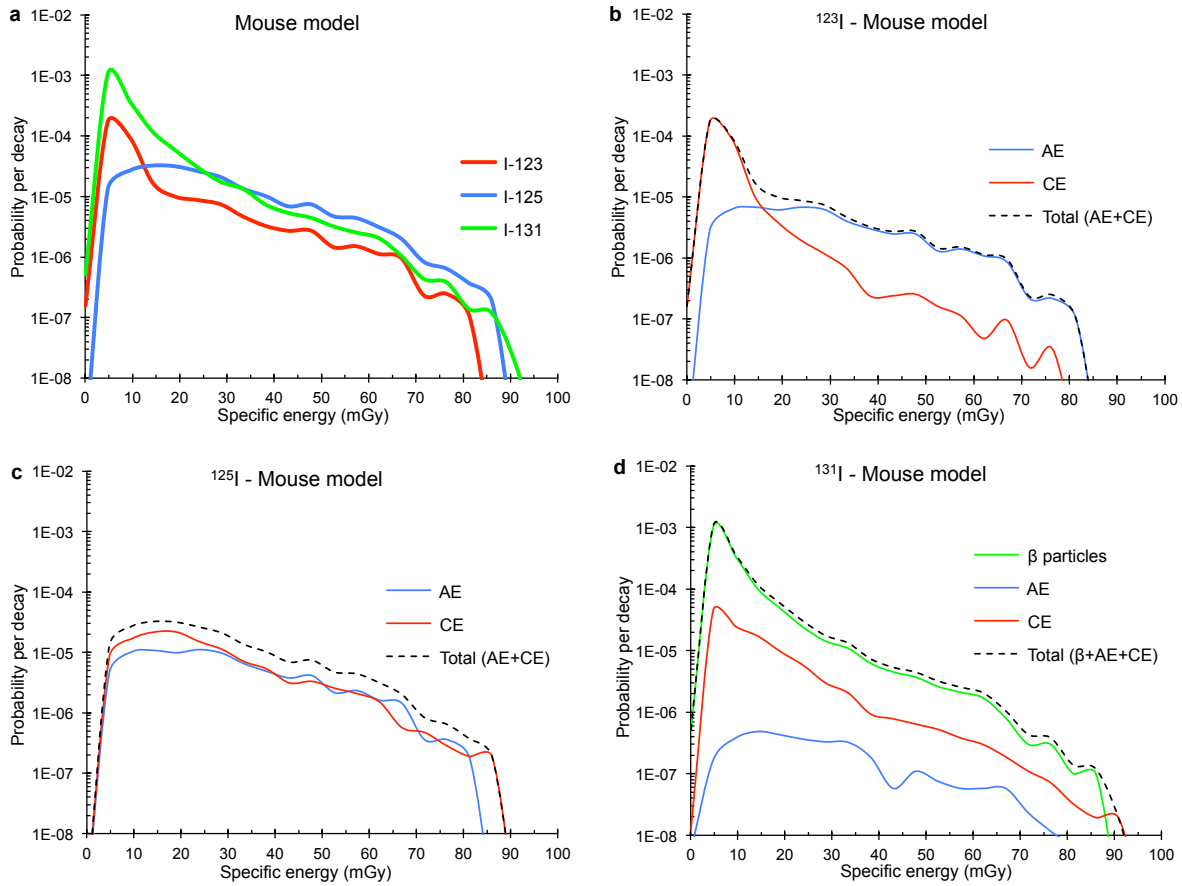

FIGURE 4.19. The specific energy distribution, *f(z),* per decay for the NR transitions (not showing the contribution from zero specific energy, z = 0) for the single follicle mouse models with radioiodine homogenously distributed within the follicle lumen. The specific energy bin size used was 4.8 mGy (1 keV), and note that the scale on the ordinate is logarithmic. **a)** The distribution of the total contribution from all the NR transitions for ^{123}I (red line), ^{125}I (blue line) and ^{131}I (green line). The specific energy distribution for **b)** ^{123}I, **c)** ^{125}I and **d)** ^{131}I showing the respective NR contributions from β^- particles (green line), AE (blue line), CE (red line) and the total contribution (black dotted line).

Figure 4.20 shows $f(z)$ per decay (not showing the contribution from z = 0) in the follicle cell nuclei for the single follicle model of rat with ^{123}I, ^{125}I and ^{131}I homogenously distributed within the follicle lumen. The maximum specific energy for ^{123}I, ^{125}I and ^{131}I were 30 mGy, 37 mGy and 41 mGy, respectively. $\langle z \rangle$ per decay for ^{123}I, ^{125}I and ^{131}I were 1.1 µGy, 1.5 µGy and 4.8 µGy, respectively.

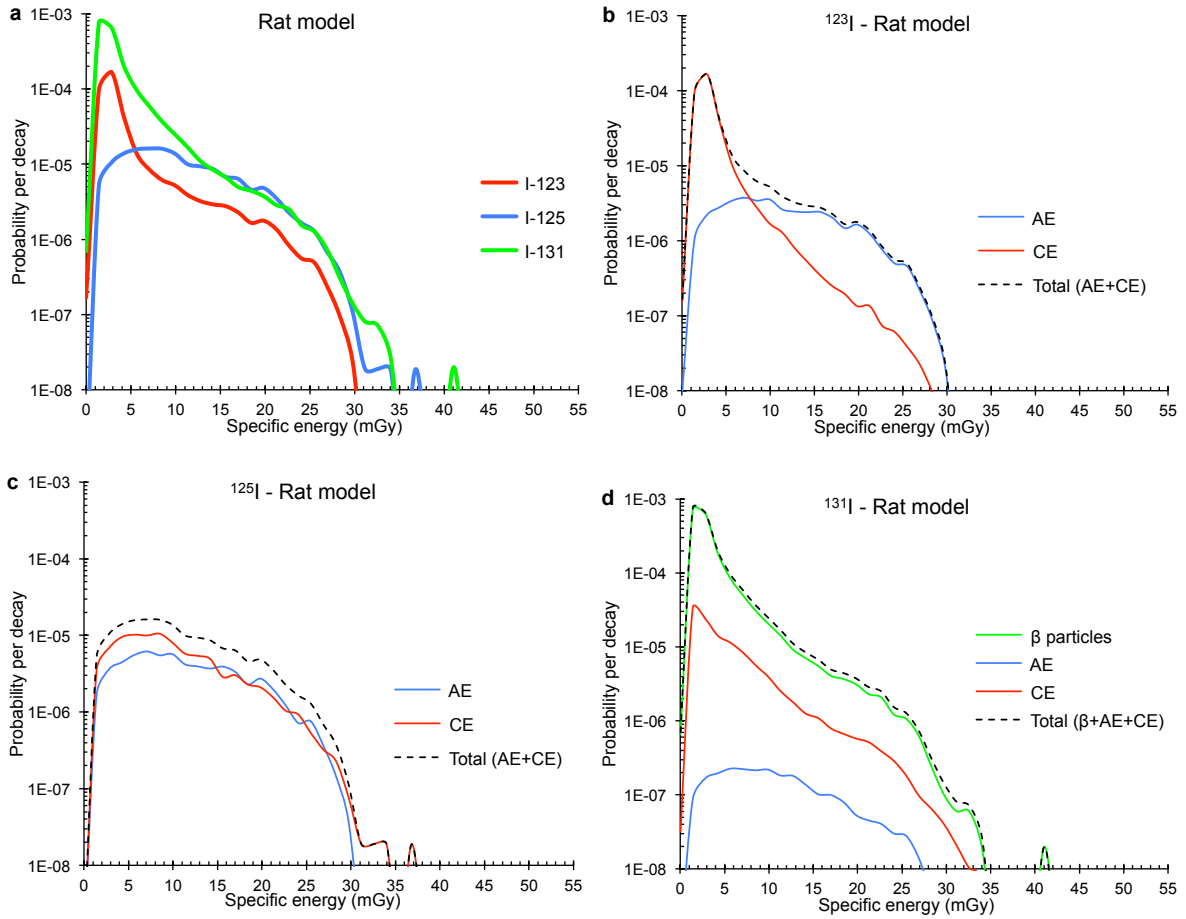

FIGURE 4.20. The specific energy distribution, *f(z),* per decay for the NR transitions (not showing the contribution from zero specific energy, z = 0) for the single follicle rat models with radioiodine homogenously distributed within the follicle lumen. The specific energy bin size used was 1.4 mGy (1 keV), and note that the scale on the ordinate is logarithmic. **a)** The distribution of the total contribution from all the NR transitions for ^{123}I (red line), ^{125}I (blue line) and ^{131}I (green line). The specific energy distribution for **b)** ^{123}I, **c)** ^{125}I and **d)** ^{131}I showing the respective NR contributions from β^- particles (green line), AE (blue line), CE (red line) and the total contribution (black dotted line).

Figure 4.21 shows $f(z)$ per decay (not showing the contribution from z = 0) in the follicle cell nuclei for the single follicle model of man with ^{123}I, ^{125}I and ^{131}I homogenously distributed within the follicle lumen. The maximum specific energy for ^{123}I, ^{125}I and ^{131}I were 14 mGy, 16 mGy and 16 mGy, respectively. $\langle z \rangle$ per decay for ^{123}I, ^{125}I and ^{131}I were 0.25 µGy, 0.14 µGy and 1.0 µGy, respectively.

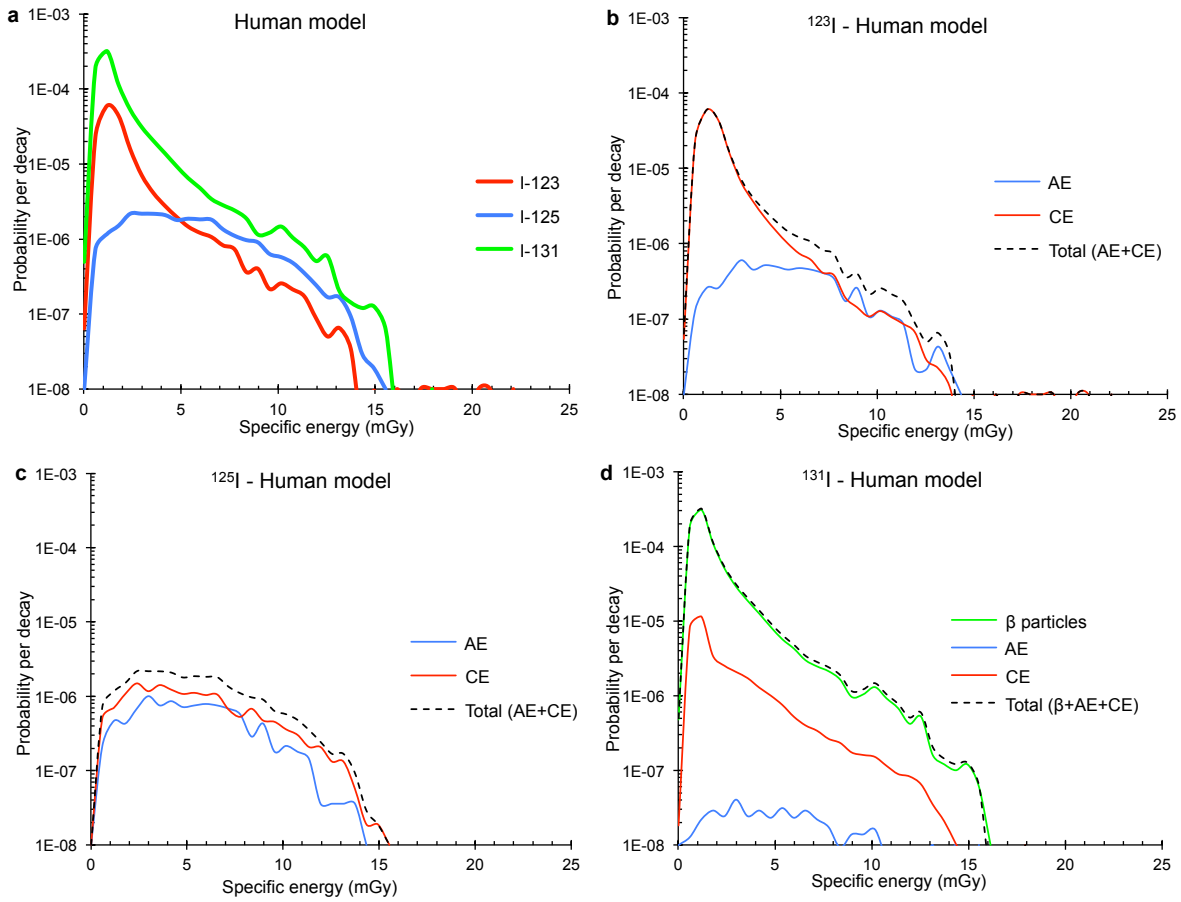

FIGURE 4.21. The specific energy distribution, *f(z),* per decay for the NR transitions (not showing the contribution from zero specific energy, z = 0) for the single follicle human models with radioiodine homogenously distributed within the follicle lumen. The specific energy bin size used was 0.6 mGy (1 keV), and note that the scale on the ordinate is logarithmic. **a)** The distribution of the total contribution from all the NR transitions for ^{123}I (red line), ^{125}I (blue line) and ^{131}I (green line). The specific energy distribution for **b)** ^{123}I, **c)** ^{125}I and **d)** ^{131}I showing the respective NR contributions from β^- particles (green line), AE (blue line), CE (red line) and the total contribution (black dotted line). (Figure 3, Paper III).

5. DISCUSSION

The dosimetric models created and used in this work were based on spherical geometry and consisted of unit density (1.0 g/cm^3) liquid water. It is common in models to approximate the composition of soft tissue and cells with unit density water in dosimetric calculations [59, 61, 63-65, 91, 92]. Concerning the thyroid gland which was the main focus in this work the tissue is composed of 78.4% water, 4.4% lipid, 14.0% protein and 2.5% other molecules (given as weight per cent), with a density of 1.05 g/cm^3 [93]. Calculations were performed to investigate the influence of stable iodine (^{127}I, density 4.94 g/cm^3) for ^{211}At in the single follicle models (Paper II). The ^{127}I was located homogeneously within the follicle lumen with a volume concentration of 1% (4% mass concentration). The result showed the presence of 1% (4% mass concentration) of ^{127}I homogeneously within the follicle lumen gave little effect on the dosimetric calculations for ^{211}At (3% in the human model). This indicates that the approximation of using unit density water in our calculations will have small effects on the results, but are probably minor compared with other assumptions made in the models.

The species-specific thyroid follicle models for mouse, rat and man were created to investigate the influence of geometry and distribution for the radiohalogens (Papers II and III). The thyroid follicles are convex entities that are closely packed within the thyroid gland (Figure 1.1). The single thyroid follicle model consisted of a central sphere representing the follicle lumen, which was surrounded by a single layer of follicle cells, with a centrally placed follicle cell nuclei (Figure 3.1). The follicle cell nuclei were chosen as the target in the thyroid follicle models, since DNA, the principal sensitive site for radiation induced cell death is located within the cell nucleus [94]. The weight of the thyroid gland varies between the different species [14-16], and there is also a variation in follicle size. E.g., in man the follicle varies between approximately 30 and 800 μm [95], and in rat between 20 and 230 μm [96, 97]. To investigate how the differences in follicles geometry affect the microdosimetric parameters average sized species-specific single thyroid follicle models were created, based on published data [14, 24, 96-99].

The species-specific multiple thyroid follicle models were developed to investigate the contributions from neighbouring follicles (Papers II and III). The number of contributing surrounding follicle layers depended on radiohalogen and species. For the radiohalogens emitting short-ranged α particles and electrons (e.g. ^{211}At and ^{125}I) only one surrounding layer of follicles contributed, while for long-ranged electrons (e.g. ^{131}I) up to 16 layers contributed (Table 3.1). The models assumed closely packed neighbouring follicles with their basal follicle cell surface (1st surrounding layer) in direct contact with the basal surface of and inner follicle (cells of the centrally located follicle, or of the surrounding follicle layers for the (2nd layer and higher). The follicle

lumens of the surrounding follicles were approximated as a spherical shell with the thickness equal to the diameter of the central follicle, and the lumen was surrounded with a single follicle cell layer (Figure 3.2). In the models no interstitial tissue was assumed, which depends on species and varies between approximately 5% and 20% [18, 89]. For ^{131}I, emitting long-ranged β particles the exclusion of interstitial tissue still resulted in similar dosimetric results compared with those of a human thyroid model by Hindié et al., consisting of 51% interstitial tissue [91]. However, for the radiohalogens emitting short-ranged electrons and α particles (e.g. ^{125}I and ^{211}At) the calculated absorbed dose would probably be somewhat overestimated in the present models. The distribution of the radiohalogens was assumed to be homogeneous within each specified source compartment or on a source surface, and the cumulative specific activity could be chosen independently in the models for the respective source compartment. This offers the possibility to perform dosimetric calculations for heterogeneous distributions of radiohalogens within the thyroid.

The choice of using the MC code MCNPX 2.6.0 [75] for the dosimetric calculations in this work was mainly based on *1)* the capabilities of simulating electrons, positrons and α particles to energies down to 1 keV, *2)* the long-term use, testing and validation of the MC code, *3)* the use of input files to which does not need major programming knowledge, *4)* the possibility of batch processing, and *5)* when this project started MCNPX 2.6.0 had recently been released.

Nuclear decay data from ICRP publication 107 [5] was used in the dosimetric calculations. ICRP 107 includes tabulated energies and intensities emitted at decay of 1252 radionuclides. The Society of Nuclear Medicine and Molecular Imaging (SNMMI) has published a monograph containing 333 radionuclides of 87 elements with interest in the field of nuclear medicine including graphical decay schemes, and are based on the same nuclear decay data as ICRP 107 [100]. Results in the present work were compared with dosimetric data obtained using MIRD nuclear decay data retrieved from their web site [90]. ICRP 107 offers the possibility of using detailed AE spectra with up to several thousands of different discrete electron energies (e.g. ^{125}I has 724 discrete energies), or conventional spectra that are condensed into groups (maximum 15) as average energies depending on radionuclide (Table 3.2). In dosimetric calculations the use of the conventional spectra are dosimetrically equivalent to the use of detailed spectrum in unit density water spheres larger than 1 μm in diameter [101]. The lowest cut-off energy in MCNPX for α particles and electrons was 1 keV, and the AE with kinetic energy of less than 1 keV were assumed to deposit all kinetic energy within the source compartment. This assumption is reasonable since the penetration range for a 1 keV electron is approximately 61 nm according to measurements by Cole in unit density matter [36], and the absorbed fraction is close to unity for 1 keV electrons homogeneously emitted within a 1 μm water sphere [102].

In the present dosimetric calculations only the NR transitions were considered, which excluded characteristic X-rays, γ-rays, annihilation photons and bremsstrahlung photons

generated by the charged particles. The generation of bremsstrahlung photons are inversely proportional to the square of the charged particle mass [39], which means for an emitted α particle from ^{211}At with a mass 7350 times heavier than an electron or positron, generation of bremsstrahlung photons can be neglected. For electrons and positrons the highest kinetic energy simulated in this work was a 3 MeV internal conversion electron (emitted by ^{124}I with very low yield), for which approximately 2.3% of the total kinetic energy is transmitted as bremsstrahlung photons [35]. These high-energy electrons/positrons have a low yield and a maximum CSDA range of approximately 1.5 cm in liquid water (Table 1), which is longer than the size of the models studied in this work. With the exception of ^{124}I, the radionuclides studied in this work emit electrons with maximum kinetic energy of approximately 1 MeV, and at that energy 0.7% of the total kinetic energy is transferred to bremsstrahlung in liquid water [35].

In the ^{211}At decay approximately 0.6% of the total energy released originate from characteristic X-rays and γ-rays (excluding the contribution from ^{207}Bi) [5], which is negligible compared with the NR transitions. For the radioiodine isotopes the photon-to-electron ratio (total energy emitted as photons divided by total energy emitted as electrons/positrons) ranged from 2.0 to 6.1 for ^{131}I and ^{123}I, respectively (Table 1.2). The main γ-ray energy and yield emitted for ^{123}I, ^{124}I, ^{125}I and ^{131}I are 159 keV (83%), 603 keV (63%), 35.5 keV (6.7%) and 364 keV (82%), respectively [5]. The mean free path (MFP) for these γ-rays are several centimetres in liquid water with the exception for ^{125}I, indicating that this contribution could be neglected in the thyroid models (MFP is the thickness of a homogenous absorber that attenuates the photon intensity to 37% of the original intensity [39]).

The emission of characteristic X-rays is a competing process to AE. ^{123}I and ^{125}I have high yields of very low energy (<1 keV) characteristic X-rays, with a maximum MFP of approximately 2.5 μm in liquid water, and is probably to a high extent deposited within the source compartment. This energy released per decay is 0.20 keV and 0.34 keV for ^{123}I and ^{125}I [5], respectively, which is low compared with the energy deposited from the NR transitions. The radioiodine isotopes ^{123}I, ^{124}I, ^{125}I and ^{131}I emit low-energy characteristic X-rays of 27.2-34.5 keV with 87%, 58%, 141% and 5% yield, respectively [5]. The MFP for a 30 keV photon is approximately 2.7 cm in liquid water, which indicates that the contribution from photons can be neglected for the present thyroid models.

The mean specific energy (S values) (Figure 4.1) and the absorbed fraction (Figure 4.2) per decay were calculated from the NR transitions for the radiohalogens ^{123}I, ^{124}I, ^{125}I, ^{131}I and ^{211}At for spheres of various sizes. The calculated ⟨z⟩ per decay in this work showed in general good agreement with previously published S values (<10% deviation) calculated with both analytic and MC methods [59, 61-66], but higher deviation was found for ^{131}I. Our results calculated using recent nuclear decay data from ICRP 107, with a well-established MC code are valuable, and could be used in crude dosimetric

estimations assuming a homogenous activity distribution. The calculations also showed the importance of using the full β particle energy spectrum in dosimetric calculations compared with the average β particle energy, with differences of up to 14% and 41% for ^{124}I and ^{131}I, respectively (Figure 4.3a and 4.3b). The difference was lower for ^{124}I, which could to some extent be explained by the lower yield (23%) of emitted β particles compared with ^{131}I (Table 1.2). Furthermore, the relative contributions from the NR transitions in subcellularly-, cellularly- and macroscopically-sized compartments were calculated for the different radiohalogens (Paper I, Figure 4 and 5a). The results indicate possible simplifications that could be used in dosimetric estimations, e.g. the use of the average α particle energy for ^{211}At (Figure 4.3c).

With ^{211}At homogenously distributed within the follicle lumen, a higher fraction of the emitted α particles deposit all their kinetic energy within the follicle lumen, not traversing the cell nuclei, for larger follicle lumen diameters. For the species-specific models of man, rat and mouse that 45%, 7% and <0.5%, respectively, of the emitted α particles deposit all their energy within the follicle lumen (Figure 4.9). This indicates that for ^{211}At distributed in the thyroid gland dosimetric parameters cannot readily be translated between species, and that there is a need for more detailed dosimetric models. Furthermore, it should also be noted that for man smaller follicles are more common in children and larger in adults [95], indicating possible differences in absorbed dose from ^{211}At in children compared with adults.

The mean absorbed dose was calculated with the species-specific multiple thyroid follicle models, and compared to calculations performed using MIRD formalism and nuclear decay data from MIRD. The energy emitted from electrons per decay from ^{123}I, ^{125}I and ^{131}I were 26.7 keV, 16.5 keV and 191.2 keV, respectively, according to MIRD [90]. The corresponding data from ICRP 107 was 28.2 keV, 19.2 keV and 191.8 keV, respectively, with a highest difference of 16% for ^{125}I [5]. This demonstrates the importance of using the most appropriate decay data when performing dosimetric calculations.

Assuming that 100% of the ^{211}At decays occurred homogenously within the follicle lumens the mean absorbed dose was 0.71, 0.84 and 0.93 Gy for the human, rat and mouse models, respectively (Figure 4.8, Table 4.1a). These results showed the largest difference in the human model compared with MIRD formalism, which overestimates the mean absorbed dose with approximately 40%. The differences were smaller in the rat (14%) and mouse (1%) models, mainly because less of the energy is absorbed within the smaller follicle lumens (Figure 4.9). In Paper II, an absorbed fraction of 1 was assumed when calculating the mean absorbed dose according to the MIRD formalism. This is a reasonable assumption due to the short range of the α particles. Including all the NR transitions in the ^{211}At decay (Paper I), and the assumption that one thyroid lobe is a homogenous sphere of unit density only containing follicles with no interstitial tissue, the calculated absorbed fraction for one thyroid lobe homogenous distribution of

^{211}At was 0.94, 0.96 and 1.0 for the mouse, rat and human models, respectively (Table 3.3).

Preclinical studies of ^{211}At performed on mice showed a heterogeneous distribution among the follicles, with up to a 20-fold difference between highest and lowest concentration 4 hours after injection [25]. Assuming a more moderate difference in concentration between follicles in the human model, with a three times higher concentration within the central follicle lumen, compared with the surrounding follicle lumen layers resulted in 30% higher mean absorbed dose. Conversely, for a three times higher concentration in the surrounding follicle lumen layers compared with the central follicle lumen, the mean absorbed dose was 50% lower.

Calculations for ^{131}I showed relatively small differences in mean absorbed dose between the different species. The largest difference was obtained for ^{125}I with its short-ranged and high yield of AE, with a mean absorbed dose of 0.11 Gy when ^{125}I was homogeneously distributed in follicle lumens in the human model, compared with 1 Gy for the same amount of ^{125}I homogeneously distributed in the entire model. This indicates that for ^{125}I distributed in the thyroid gland dosimetric parameters cannot readily be translated between species, and that there is a need for detailed dosimetric models for other heterogeneous tissues.

For a peripherally located follicle in the thyroid gland, fewer surrounding follicles will contribute to the absorbed dose. This will probably have the largest effect for ^{131}I with contribution from many surrounding layers due to the long-range β particles. The contribution from the central follicle was about 7%, in the model of man for a homogenous distribution within the follicle lumens. Concerning ^{125}I and ^{211}At with their short-ranged electrons and α particles, the contribution from the central follicle was 94% and 45%, respectively. This implies that heterogeneous distributions within the thyroid gland for ^{125}I and ^{211}At could result in large differences in absorbed dose.

When the emitted α particle traverses the cell nucleus the specific energy depends on, e.g. path length through the nucleus and kinetic energy of the α particle (Figure 1.2b). In the human model the specific energy per decay when emitted from the follicle lumen varied between 0 and 1 Gy (Figure 4.7), with $\langle z \rangle$ per decay equal to 0.17 mGy, and $\langle z_1 \rangle$ per decay equal to 0.37 Gy (Paper II). This demonstrates the possibility of large individual difference in absorbed dose to different cell nuclei, including cell nuclei with no absorbed dose. It also shows that on average only three α particles are needed to traverse the cell nucleus to achieve a mean absorbed dose of 1 Gy. For β particles emitted by ^{131}I, with $\langle z \rangle$ per decay equal to 1.0 μGy, and $\langle z_1 \rangle$ per decay equal to 1.3 mGy, approximately 800 β particles need to traverse the follicle cell nucleus to achieve a mean absorbed of 1 Gy.

The data from the multiple thyroid follicle models developed in this work can be applied in a flexible way. It is possible to choose different distribution and concentration of the

radiohalogens in the different source compartments (follicle lumens and/or follicle cells), and calculate ⟨z⟩ per decay from the results given in this work. Furthermore, calculations performed for different surface sources allow the possibility for non-homogenous distributions within the follicle lumens, e.g. for decays occurring at the apical cell surface or at other specific locations within the follicle lumens.

6. Conclusions And Future Directions

The mean specific energy per decay (equivalent to S value) for unit density spheres of different sizes were calculated for the radiohalogens ^{123}I, ^{124}I, ^{125}I, ^{131}I and ^{211}At using recent nuclear decay data from ICRP 107. The results showed in general good agreement (<10% deviation) with data obtained using previously published nuclear decay data based on both analytical and MC methods. Larger deviations were only found for ^{131}I. Absorbed fraction for the spheres was calculated for the NR transitions in the decay of the radiohalogens. Furthermore, the relative contribution from the NR transitions (AE, CE, and β and α particles) for the radiohalogens was determined at subcellular, cellular and macroscopic levels.

Results using the average β particle energy compared with the full beta spectrum showed differences in mean specific energy and mean absorbed dose of up to 40% for ^{131}I and 14% for ^{124}I. Thus, it might be important to use more detailed decay data than the average energy for emitted beta particles at certain applications.

For ^{211}At the use of the average α particle energy is adequate for dosimetric calculations, with a maximum deviation of 5% compared with the use of the complete decay data including all seven possible α particles energies, AE and CE.

Species-specific thyroid follicle models were developed for mouse, rat and man, based on geometric information from the literature. Both single follicle models and multiple follicle models were defined. The models are realistic but relatively simple in geometry, which makes them useful for Monte Carlo simulations.

Calculations performed for ^{211}At in the species-specific single thyroid follicle models showed that difference in energy deposition depends on the location of the emitted α particle and the size of the follicle, showing the importance of species-specific models for dosimetric calculations. Dosimetric calculations for homogeneous distribution of ^{211}At within the thyroid gland (MIRD formalism) compared with the species-specific multiple thyroid follicle models for a heterogeneous distribution showed differences of up to 40%.

Calculations performed for ^{125}I using MIRD formalism and previous nuclear decay data showed differences in mean absorbed dose of up to 800% compared with the multiple thyroid follicle models for a heterogeneous radionuclide distribution, and 15% for a homogeneous distribution within the human thyroid gland. Corresponding differences were 25% and 2% for ^{123}I and ^{131}I for heterogeneous and 8% and 4% for homogeneous radionuclide distribution, respectively.

Altogether, the dosimetric data determined for these thyroid follicle models for ^{123}I, ^{125}I, ^{131}I and ^{211}At allow the possibility to more easily estimate dosimetric parameters for

different radiohalogen distributions, both heterogeneous and homogeneous, and activity concentrations in the compartments of these models.

Although the focus of this work was on radiohalogens in the thyroid, the results show that it might be important to perform microdosimetric calculations for other inhomogeneous tissue types and radionuclides emitting relatively short-ranged particles. To further improve such dosimetric calculations, detailed knowledge of the radionuclide distribution as a function of time at macroscopic, cellular, and subcellular levels is needed. To determine biokinetics of the radionuclides autoradiographical imaging techniques have proven to be useful.

7. ACKNOWLEDGEMENTS

I would like to thank my family, friends and colleagues at the Department of Radiation Physics who have helped and supported me through this roller coaster ride as a PhD-student, especially the following

My supervisor, Professor **Eva Forssell-Aronsson**, for introducing me to research and giving me the opportunity to learn more about this subject, and for her constructive support.

My co-supervisor, Professor **Peter Bernhardt**, for the support in the beginning and end.

A very warm thanks to my roommates **Maria** and **Johanna** for being great friends, always taking the time to discus life and science over a cup of coffee, will miss you. **Micke** for all the fun times, first as students at the Medical Physics program, and then as PhD-students. **Angelica** for setting the standard. **Jenny** for all the help, being the only one I could discuss Monte Carlo with. **Lilian** for all the help with the experiments, and the morning coffee company. **Esmaeil** for the philosophical and humoristic discussions. **Tom** whom I am sure had some part in getting me the position at Johns Hopkins, **Niclas**, **Johan**, **Nils**, **Emil**, **Britta, Elin, Anna, Ann, Mia, Lars, Gunilla** and other colleges and PhD-students at the Department.

My mother **Lisbeth** for always being there, **Sören**, **Krister, Sofie**, **Eva**, **Magnus**, **Mattias**, **Anders**, **Björn**, **Brad**, **John**...

Financial support was provided by grants from the European Commission FP7 Collaborative Project TARCC HEALTH-F2-2007-201962, the Swedish Research Council, the Swedish Cancer Society, BioCARE, a National Strategic Research Program at University of Gothenburg, the Swedish Radiation Safety Authority, the King Gustav V Jubilee Clinic Cancer Research Foundation and the Assar Gabrielsson Cancer Research Foundation.

Two hydrogen atoms walk into a bar.
One says, “I think I’ve lost an electron.”
The other says, “Are you sure?”
The first replies, “Yes, I’m positive…”

8. REFERENCES

1. Seidlin, S.M., L.D. Marinelli, and E. Oshry, *Radioactive iodine therapy; effect on functioning metastases of adenocarcinoma of the thyroid.* J Am Med Assoc, 1946. **132**(14): p. 838-47.
2. Hamilton, J.G., P.W. Durbin, and M.W. Parrott, *Accumulation of astatine-211 by thyroid gland in man.* Proc. Soc. Exp. Biol. Med., 1954. **86**: p. 366-369.
3. Zalutsky, M.R., et al., *Clinical experience with alpha-particle emitting 211At: treatment of recurrent brain tumor patients with 211At-labeled chimeric antitenascin monoclonal antibody 81C6.* J Nucl Med, 2008. **49**(1): p. 30-8.
4. Andersson, H., et al., *Intraperitoneal alpha-particle radioimmunotherapy of ovarian cancer patients: pharmacokinetics and dosimetry of (211)At-MX35 F(ab')2--a phase I study.* J Nucl Med, 2009. **50**(7): p. 1153-60.
5. Valentin, J., *ICRP Publication 107: Nuclear decay data for dosimetric calculations*. Vol. 38. 2009, Oxford: Published for the International Commission on Radiological Protection by Elsevier.
6. Morzenti, S., et al., *Cyclotron production of At-211/Po-211g by Bi-209(α,2n) reaction.* Journal of Radioanalytical and Nuclear Chemistry, 2008. **276**(3): p. 843-847.
7. Spetz, J., N. Rudqvist, and E. Forssell-Aronsson, *Biodistribution and Dosimetry of Free 211At, 125I- and 131I- in Rats.* Cancer Biother Radiopharm, 2013. **28**(9): p. 657-664.
8. Lundh, C., et al., *Biodistribution of free 211At and 125I- in nude mice bearing tumors derived from anaplastic thyroid carcinoma cell lines.* Cancer Biother Radiopharm, 2006. **21**(6): p. 591-600.
9. Hamilton, J.G. and M.H. Soley, *A Comparison of the Metabolism of Iodine and of Element 85 (Eka-Iodine).* Proc Natl Acad Sci U S A, 1940. **26**(8): p. 483-489.
10. Hamilton, J.G., et al., *The accumulation, metabolism, and biological effects of astatine in rats and monkeys.* Univ. Calif. (Berkeley) Publs. Pharmacol., 1953. **2**(21): p. 283-344.
11. Hamilton, J.G., P.W. Durbin, and M. Parrott, *The accumulation and destructive action of astatine-211 (eka-iodine) in the thyroid gland of rats and monkeys.* Journal of Clinical Endocrinology & Metabolism, 1954. **14**(10): p. 1161-1178.
12. Cobb, L.M., et al., *Relative concentration of astatine-211 and iodine-125 by human fetal thyroid and carcinoma of the thyroid in nude mice.* Radiother Oncol, 1988. **13**(3): p. 203-9.
13. Berg, G., et al., *Tyreoideasjukdomar hos vuxna*. 2007, Stockholm: Nycomed.
14. Clement, S., et al., *Low TSH requirement and goiter in transgenic mice overexpressing IGF-I and IGF-Ir receptor in the thyroid gland.* Endocrinology, 2001. **142**(12): p. 5131-9.

15. Soukup, T., et al., *Body, heart, thyroid gland and skeletal muscle weight changes in rats with altered thyroid status.* Physiol Res, 2001. **50**(6): p. 619-26.
16. Bisi, H., et al., *The prevalence of unsuspected thyroid pathology in 300 sequential autopsies, with special reference to the incidental carcinoma.* Cancer, 1989. **64**(9): p. 1888-93.
17. Snyder, W.S., et al., *ICRP Publication 23: Report of the task group on reference man*. Vol. 23. 1975: Pergamon Oxford.
18. Malone, J.F., *The radiation biology of the thyroid.* Curr Top Radiat Res Q, 1975. **10**(4): p. 263-368.
19. Gillam, M.P., et al., *Functional characterization of pendrin in a polarized cell system. Evidence for pendrin-mediated apical iodide efflux.* J Biol Chem, 2004. **279**(13): p. 13004-10.
20. Lindencrona, U., M. Nilsson, and E. Forssell-Aronsson, *Similarities and differences between free 211At and 125I- transport in porcine thyroid epithelial cells cultured in bicameral chambers.* Nucl Med Biol, 2001. **28**(1): p. 41-50.
21. Cobb, L.M., A. Harrison, and S.A. Butler, *Toxicity of astatine-211 in the mouse.* Human toxicology, 1988. **7**(6): p. 529.
22. Hamilton, J.G., et al., *The destruction of thyroid tissue in the rat by the halogen, astatine.* J Clin Invest, 1950. **29**(6): p. 820.
23. Harrison, A. and L. Royle, *Determination of Absorbed Dose to Blood, Kidneys, Testes and Thyroid in Mice Injected With 211At and Comparison of Testes Mass and Sperm Number in X-irradiated and 211At Treated Mice.* Health physics, 1984. **46**(2): p. 377.
24. Nadler, N.J., C.P. Leblond, and R. Bogoroch, *The rate of iodine metabolism by the thyroid follicle as a function of its size.* Endocrinology, 1954. **54**(2): p. 154-72.
25. Cobb, L.M., S.A. Butler, and A. Harrison, *The effect of the alpha-particle emitter astatine-211 in the mouse at the minimum toxic dose.* Hum Exp Toxicol, 1990. **9**(5): p. 289-93.
26. Fujita, H., *Studies on the iodine metabolism of the thyroid gland as revealed by electron microscopic autoradiography of 125I.* Virchows Archiv. B: Cell pathology, 1969. **2**(4): p. 265-79.
27. Loewenstein, J.E. and S.H. Wollman, *Diffusion of thyroglobulin in the lumen of rat thyroid follicle.* Endocrinology, 1967. **81**(5): p. 1086-90.
28. Loewenstein, J.E. and S.H. Wollman, *Distribution of organic 125-I and 127-I in the rat thyroid gland during equilibrium labeling as determined by autoradiography.* Endocrinology, 1967. **81**(5): p. 1074-85.
29. Leblond, C.P. and J. Gross, *Thyroglobulin formation in the thyroid follicle visualized by the coated autograph technique.* Endocrinology, 1948. **43**(5): p. 306-24.
30. Wollman, S.H. and I. Wodinsky, *Localization of protein-bound I131 in the thyroid gland of the mouse.* Endocrinology, 1955. **56**(1): p. 9-20.
31. Ekholm, R. and S.H. Wollman, *Site of iodination in the rat thyroid gland deduced from electron microscopic autoradiographs.* Endocrinology, 1975. **97**(6): p. 1432-44.

32. Sheldon, H., J.M. McKenzie, and D. Vannimwegan, *Electron Microscopic Autoradiography: The Localization of I-125 in Suppressed and Thyrotropin-Stimulated Mouse Thyroid Gland.* J Cell Biol, 1964. **23**: p. 200-5.
33. Andros, G. and S.H. Wollman, *Autoradiography of Diffusible Ions with Application to Thyroidal Radioiodide.* J Histochem Cytochem, 1965. **13**: p. 390-5.
34. Andros, G. and S.H. Wollman, *Autoradiographic localization of radioiodide in the thyroid gland of the mouse.* Am J Physiol, 1967. **213**(1): p. 198-208.
35. ICRU, *ICRU Report 37: Stopping Power for Electrons and Positrons*. ICRU Report 37. 1984, Bethesda, MD: International Commission on Radiation Units and Measurements. x, 271 p.
36. Cole, A., *Absorption of 20-eV to 50,000-eV electron beams in air and plastic.* Rad Res, 1969. **38**(1): p. 7-33.
37. ICRU, *ICRU Report 49: Stopping powers and ranges for protons and alpha particles*. ICRU Report 49. 1993, Bethesda, MD: International Commission on Radiation Units and Measurements. x, 286 p.
38. Meitner, L., *Über die Entstehung der β-Strahl-Spektren radioaktiver Substanzen.* Zeitschrift für Physik, 1922. **9**(1): p. 131-144.
39. Podgorsak, E.B., *Radiation physics for medical physicists, second edition*. 2010: Springer Verlag.
40. Coster, D. and R.D. L. Kronig, *New type of auger effect and its influence on the x-ray spectrum.* Physica, 1935. **2**(1–12): p. 13-24.
41. Charlton, D.E. and J. Booz, *A Monte Carlo treatment of the decay of 125I.* Rad Res, 1981. **87**(1): p. 10-23.
42. Kassis, A.I., *The amazing world of auger electrons.* International journal of radiation biology, 2004. **80**(11-12): p. 789-803.
43. Janni, J.F., *Calculations of energy loss, range, pathlength, straggling, multiple scattering, and the probability of inelastic nuclear collisions for 0.1-to 1000-MeV protons*. 1966: DTIC Document.
44. Krane, K.S. and D. Halliday, *Introductory nuclear physics*. 1987, New York: Wiley. xiii, 845 p.
45. Jardine, L.J., *Decays of 211-At, 211-Po, and 207-Bi.* Physical Review C, 1975. **11**(4): p. 1385.
46. Center., N.N.D. *Interactive chart of nuclides*. 2014; Available from: http://www.nndc.bnl.gov/chart/.
47. ICRP, R.T., *Energy and Intensity of Emissions. Publication 38, International Commission on Radiological Protection*. 1983, Pergamon Press, New York.
48. Uusijarvi, H., P. Bernhardt, and E. Forssell-Aronsson, *Translation of dosimetric results of preclinical radionuclide therapy to clinical situations: influence of photon irradiation.* Cancer Biother Radiopharm, 2007. **22**(2): p. 268-74.
49. Corson, D.R., K.R. MacKenzie, and E. Segré, *Artificially Radioactive Element 85.* Physical Review, 1940. **58**(8): p. 672-678.
50. Corson, D.R., K.R. MacKenzie, and E. Segré, *Astatine : The element of atomic number 85.* Nature, 1947. **159**: p. 24.

51. Mansi, L., et al., *Nuclear medicine in diagnosis, staging and follow-up of thyroid cancer.* Q J Nucl Med Mol Imaging, 2004. **48**(2): p. 82-95.
52. Hauser, R.A. and D.G. Grosset, *[123I]FP-CIT (DaTscan) SPECT brain imaging in patients with suspected parkinsonian syndromes.* Journal of neuroimaging : official journal of the American Society of Neuroimaging, 2012. **22**(3): p. 225-30.
53. Belov, V.V., et al., *Iodine-124 as a label for pharmacological PET imaging.* Mol Pharm, 2011. **8**(3): p. 736-47.
54. Freudenberg, L.S., et al., *Clinical applications of 124I-PET/CT in patients with differentiated thyroid cancer.* Eur J Nucl Med Mol Imaging, 2011. **38 Suppl 1**: p. S48-56.
55. Harkrider, W.W., et al., *An extended phase II trial of iodine-125 methylene blue for sentinel lymph node identification in women with breast cancer.* Journal of the American College of Surgeons, 2013. **216**(4): p. 599-605; discussion 605-6.
56. Tomblyn, M., *Radioimmunotherapy for B-cell non-Hodgkin lymphomas.* Cancer control : journal of the Moffitt Cancer Center, 2012. **19**(3): p. 196-203.
57. ICRU, *ICRU Report 85: Fundamental Quantities and Units for Ionizing Radiation*. 2011/04/01 ed. J ICRU. Vol. 11. 2011.
58. Loevinger, R., T.F. Budinger, and E.E. Watson, *MIRD Primer for absorbed dose calculations*. 1991: The Society of Nuclear Medicine New York.
59. Goddu, S.M. and T.F. Budinger, *MIRD Cellular S. Values: Self-absorbed Dose Per Unit Cumulated Activity for Selected Radionuclides and Monoenergetic Electron and Alpha Particle Emitters Incorporated Into Different Cell Compartments*. 1997: Society of Nuclear Medicine Reston, VA.
60. Bolch, W.E., et al., *MIRD pamphlet No. 21: a generalized schema for radiopharmaceutical dosimetry--standardization of nomenclature.* J Nucl Med, 2009. **50**(3): p. 477-84.
61. Goddu, S.M., D.V. Rao, and R.W. Howell, *Multicellular dosimetry for micrometastases: dependence of self-dose versus cross-dose to cell nuclei on type and energy of radiation and subcellular distribution of radionuclides.* J Nucl Med, 1994. **35**(3): p. 521-30.
62. Goddu, S.M., R.W. Howell, and D.V. Rao, *Cellular dosimetry: absorbed fractions for monoenergetic electron and alpha particle sources and S-values for radionuclides uniformly distributed in different cell compartments.* J Nucl Med, 1994. **35**(2): p. 303-16.
63. Bardies, M. and J.F. Chatal, *Absorbed doses for internal radiotherapy from 22 beta-emitting radionuclides: beta dosimetry of small spheres.* Phys Med Biol, 1994. **39**(6): p. 961-81.
64. Stinchcomb, T. and J. Roeske, *Values of" S,"$< z_1 >$, and $<(z_1)^2>$ for dosimetry using alpha-particle emitters.* Med Phys, 1999. **26**(9): p. 1960-71.
65. Champion, C., P. Zanotti-Fregonara, and E. Hindie, *CELLDOSE: a Monte Carlo code to assess electron dose distribution--S values for 131I in spheres of various sizes.* J Nucl Med, 2008. **49**(1): p. 151-7.

66. Li, W.B., et al., *Track structures and dose distributions from decays of (131)I and (125)I in and around water spheres simulating micrometastases of differentiated thyroid cancer.* Rad Res, 2001. **156**(4): p. 419-29.
67. Hindorf, C., et al., *Change in tumor-absorbed dose due to decrease in mass during fractionated radioimmunotherapy in lymphoma patients.* Clin Cancer Res, 2003. **9**(10 Pt 2): p. 4003S-6S.
68. Kellerer, A.M. and D. Chmelevsky, *Criteria for the applicability of LET.* Rad Res, 1975. **63**(2): p. 226-34.
69. Sgouros, G., et al., *MIRD Pamphlet No. 22 (abridged): radiobiology and dosimetry of alpha-particle emitters for targeted radionuclide therapy.* J Nucl Med, 2010. **51**(2): p. 311-28.
70. Rossi HH., *Microdosimetric energy distribution in irradiated matter.*, in *Radiation dosimetry Vol I Fundamentals*, Attix FH., Roesch WC., and Tochilin E., Editors. 1968, Academic Press: New York. p. 43-89.
71. International Commission on Radiation Units and Measurements., *ICRU Report 36: Microdosimetry*. ICRU Report 36. 1983, Bethesda, Md., U.S.A.: International Commission on Radiation Units and Measurements. ix, 118 p.
72. Cauchy, A., *Memoire sur la rectification des courbes et la quadrature des sourface courbe. In (ed): Oevres Complétes d'Augustin Cauchy.* Paris: Gauthier-Villars, 1908.
73. X-5 MONTE CARLO TEAM, *MCNP - A General Monte Carlo N-Particle Transport Code, Version 5 - Volume I: Overview and Theory, LA-UR-03-1987*. 2003, Los Alamos National Laboratory.
74. de Buffon, G., *Essai d'arithmétique morale.* Supplément á l'Histoire Naturelle, 1777. **4**.
75. D. B. Pelowitz, *MCNPX, User's Manual Version 2.6.0. LA-CP-07-1473*. 2008, Los Alamos National Laboratory.
76. Los Alamos National Laboratory. *MCNP6 - A general Monte Carlo N-Particle (MCNP) Transport Code*. 2013; Available from: https://mcnp.lanl.gov/.
77. National Research Council Canada. *Electron Gamma Shower (EGS) software tool to model radiation transport*. 2013; Available from: http://www.nrc-cnrc.gc.ca/eng/solutions/advisory/egsnrc_index.html.
78. Kawrakow I and Rogers DW, *The EGSnrc code system: Monte Carlo simulations electron and photon transport.* NRCC Report PIRS-701, 2001.
79. Salvat F, Fernández-Varea JM, and Sempau J, *PENELOPE-2011: A code system for Monte Carlo Simulation of electron and photon transport*. 2011: In Paris: OECD Nuclear energy agency.
80. Agostinelli S, Allison J, and Amako K, *GEANT4 - a simulation toolkit.* Nucl Instruments Meth Phys Res A, 2003. **506**(3).
81. consultants, V.e. *The visual editor*. 2013; Available from: http://www.mcnpvised.com/.
82. science, W.r. *Moritz geometry tool*. 2013; Available from: http://www.whiterockscience.com/moritz.html.

83. Waters, L.S., et al., *The MCNPX Monte Carlo Radiation Transport Code.* AIP Conference Proceedings, 2007. **896**(1): p. 81-90.
84. Berger, M.J., *"Monte Carlo Calculations of the Penetration and Diffusion of Fast Charged Particles." In: Methods in Computational Physics, Vol. 1.*, ed. B.F. Alder, S. Rotenberg, M. 1963, New York: Academic Press.
85. Landau, L., *On the Energy Loss of Fast Particles by Ionization.* J Phys (USSR), 1944. **8**: p. 201.
86. Blunk, O. and S. Leisegang, *Zum Energieverlust schneller Elektronen in dünnen Schichten.* Z Physik, 1950. **128**: p. 500.
87. Goudsmit, S. and J.L. Saunderson, *Multiple Scattering of Electrons.* Phys Rev, 1940. **57**: p. 24-29.
88. Los Alamos National Laboratory. *MCNP - A general Monte Carlo N-particle transport code - Version 5*. 2005; Available from: https://mcnp.lanl.gov/.
89. Dumont, J.E., et al., *Physiological and pathological regulation of thyroid cell proliferation and differentiation by thyrotropin and other factors.* Physiol Rev, 1992. **72**(3): p. 667-97.
90. National Nuclear Data Center. *Nuclear decay data in the MIRD format*. Available from: http://www.nndc.bnl.gov/mird/.
91. Hindie, E., et al., *Calculation of electron dose to target cells in a complex environment by Monte Carlo code "CELLDOSE".* Eur J Nucl Med Mol Imaging, 2009. **36**(1): p. 130-6.
92. Bousis, C., D. Emfietzoglou, and H. Nikjoo, *Monte Carlo single-cell dosimetry of I-131, I-125 and I-123 for targeted radioimmunotherapy of B-cell lymphoma.* International journal of radiation biology, 2012. **88**(12): p. 908-15.
93. Woodard, H.Q. and D.R. White, *The composition of body tissues.* Br J Radiol, 1986. **59**(708): p. 1209-18.
94. Hall, E.J., *Radiobiology for the radiologist*. 7th ed. 2012, Philadelphia ; London: Lippincott Williams & Wilkins. xi, 588 p.
95. Faggiano, A., et al., *Age-dependent variation of follicular size and expression of iodine transporters in human thyroid tissue.* J Nucl Med, 2004. **45**(2): p. 232-7.
96. Uchiyama, Y., A. Oomiya, and G. Murakami, *Fluctuations in follicular structures of rat thyroid glands during 24 hours: fine structural and morphometric studies.* Am J Anat, 1986. **175**(1): p. 23-33.
97. Penel, C., et al., *Stereological analysis of thyroid follicle structure.* Experientia, 1981. **37**(9): p. 1010-2.
98. Friedrichs, B., et al., *Thyroid functions of mouse cathepsins B, K, and L.* J Clin Invest, 2003. **111**(11): p. 1733-45.
99. Jackson, J.L., *The shape and size of the human thyroid follicle in health and disease.* The anatomical record, 1931. **48**(2): p. 219-39.
100. Eckerman, K.F. and A. Endo, *MIRD Radionuclide Data and Decay Schemes*. 2007. Medium: X.

101. Howell, R.W., *Radiation spectra for Auger-electron emitting radionuclides: report No. 2 of AAPM Nuclear Medicine Task Group No. 6.* Med Phys, 1992. **19**(6): p. 1371-83.
102. Bousis, C., D. Emfietzoglou, and H. Nikjoo, *Calculations of absorbed fractions in small water spheres for low-energy monoenergetic electrons and the Auger-emitting radionuclides (123)I and (125)I.* International journal of radiation biology, 2012. **88**(12): p. 916-21.